

The infrared to X-ray correlation spectra of unobscured type 1 active galactic nuclei

I. García-Bernete,^{1,2*} C. Ramos Almeida,^{1,2} H. Landt,³ M. J. Ward,³ M. Baloković⁴ and J. A. Acosta-Pulido^{1,2}.

¹*Instituto de Astrofísica de Canarias, Calle Vía Láctea, s/n, E-38205, La Laguna, Tenerife, Spain*

²*Departamento de Astrofísica, Universidad de La Laguna, E-38206, La Laguna, Tenerife, Spain*

³*Centre for Extragalactic Astronomy, Department of Physics, Durham University, South Road, Durham DH1 3LE, UK*

⁴*Cahill Center for Astronomy and Astrophysics, California Institute of Technology, 1216 E California Blvd, Pasadena, CA 91125, USA*

ABSTRACT

We use new X-ray data obtained with the *Nuclear Spectroscopic Telescope Array (NuSTAR)*, near-infrared (NIR) fluxes, and mid-infrared (MIR) spectra of a sample of 24 unobscured type 1 active galactic nuclei (AGN) to study the correlation between various hard X-ray bands between 3 and 80 keV and the infrared (IR) emission. The IR to X-ray correlation spectrum (IRXCS) shows a maximum at $\sim 15\text{--}20\ \mu\text{m}$, coincident with the peak of the AGN contribution to the MIR spectra of the majority of the sample. There is also a NIR correlation peak at $\sim 2\ \mu\text{m}$, which we associate with the NIR bump observed in some type 1 AGN at $\sim 1\text{--}5\ \mu\text{m}$ and is likely produced by nuclear hot dust emission. The IRXCS shows practically the same behaviour in all the X-ray bands considered, indicating a common origin for all of them. We finally evaluated correlations between the X-ray luminosities and various MIR emission lines. All the lines show a good correlation with the hard X-rays ($\rho \geq 0.7$), but we do not find the expected correlation between their ionization potentials and the strength of the IRXCS.

Key words: galaxies: active – galaxies: photometry – galaxies: spectroscopy – infrared: galaxies – X-rays: galaxies

1 INTRODUCTION

Active galactic nuclei (AGN) are powered by accretion of material onto supermassive black holes (SMBHs), which release energy in the form of radiation and/or mechanical outflows into the host galaxy’s interstellar medium. This feedback process appears to be fundamental to the formation and evolution of galaxies (Hopkins & Quataert 2010). Therefore, it is important to characterize the properties of AGN in the local universe to understand how they are triggered and whether all galaxies with SMBHs go through an active phase.

Due to the high energies involved in the accretion process, AGN are strong X-ray emitters. This emission is mainly produced by the Comptonization of accretion disc photons in a hot corona of electrons surrounding the SMBH (e.g., Haardt & Maraschi 1991). On the other hand, the unified model of AGN proposes that there is dust surrounding the active nucleus distributed in a toroidal geometry (Antonucci 1993) which obscures the central engines of type 2 AGN, and

allows a direct view in the case of type 1 sources. Previous X-ray studies confirmed this scheme since, in general, type 2s have higher absorption column densities than type 1 AGN (e.g., Awaki et al. 1991; Smith & Done 1996; Turner et al. 1997; Bassani et al. 1999; Cappi et al. 2006; Dadina 2008; Ricci et al. 2011; Singh, Shastri, & Risaliti 2011). Although some exceptions have been observed (e.g., Cappi et al. 2006; de Rosa et al. 2007; Corral et al. 2011), those are expected if the broad line region (BLR) and the dusty torus have a clumpy distribution (see e.g., Elitzur 2012 and references therein).

High energy X-ray observations of active galaxies enable studies of the intrinsic emission from the central engine since: 1) they are less sensitive to the effects of obscuration than softer X-ray energies, and 2) very high energies are involved in the accretion process. The main source of X-ray emission is the intrinsic AGN continuum, which is observed from $\sim 1\ \text{keV}$ to over 100 keV. This primary X-ray emission can be reflected (e.g., inverse Compton scattering of photons from the accretion disc; Jovanović et al. 2008) and the main features of this reflection component are the so-called “Compton hump”, which peaks at $\sim 30\ \text{keV}$

* E-mail: igarcia@iac.es

(George & Fabian 1991), and the Fe K α fluorescence line at 6.4 keV. The Compton hump is produced by the reprocessing of X-ray photons by Compton-thick material, but the exact location of such material (the corona, the BLR and/or the torus) is not clear.

The dusty torus absorbs the intrinsic AGN radiation, and then reprocesses it to emerge in the infrared (IR), peaking in the mid-IR (MIR; $\sim 5\text{--}30\ \mu\text{m}$) according to torus models (e.g., Pier & Krolik 1992). Thus, MIR observations of active galaxies are key to study the emission of dust heated by the AGN, but also by star-formation (SF) when present (e.g., Radomski et al. 2003; Packham et al. 2005; Sales et al. 2013; Esquej et al. 2014; Alonso-Herrero et al. 2014; Ramos Almeida et al. 2014; Ruschel-Dutra et al. 2014; García-Bernete et al. 2015). The main spectral features of AGN in the MIR are the silicates, the polycyclic aromatic hydrocarbon (PAH) emission bands, and several emission lines of different ionization potential (IP).

The PAH features are often used to measure the star formation rate (SFR) of galaxies (see e.g., Peeters, Spoon, & Tielens 2004; Wu et al. 2005; Diamond-Stanic & Rieke 2012; Esquej et al. 2014), together with low IP MIR emission lines such as [Ne II] $\lambda 12.81\ \mu\text{m}$ and [S III] $\lambda 18.71\ \mu\text{m}$ (Spinoglio & Malkan 1992; Spinoglio et al. 2012; Ho & Keto 2007; Pereira-Santaella et al. 2010b). On the other hand, the presence and strengths of high IP emission lines such as [Ne V] $\lambda 14.32\ \mu\text{m}$ ($\sim 97\ \text{eV}$) and [O IV] $\lambda 25.89\ \mu\text{m}$ ($\sim 55\ \text{eV}$) are considered to be reliable indicators of the AGN power. The [O IV] emission line has proved to be a reliable AGN tracer (see e.g., García-Bernete et al. 2016 and references therein), which correlates well with both the hard X-rays (Meléndez et al. 2008a; Rigby, Diamond-Stanic, & Aniano 2009; Diamond-Stanic, Rieke, & Rigby 2009) and the soft X-rays (Prieto, Pérez García, & Rodríguez Espinosa 2002). Another AGN tracer commonly used is the [S IV] $\lambda 10.51\ \mu\text{m}$ line (IP $\sim 35\ \text{eV}$; Dasyra et al. 2011). However, this emission line can also be produced in star forming regions, as shown by Pereira-Santaella et al. (2010a). The same applies to the [Ne III] $\lambda 15.56\ \mu\text{m}$ (IP $\sim 41\ \text{eV}$) emission line (Ho & Keto 2007; Gorjian et al. 2007; Meléndez et al. 2008a; Pereira-Santaella et al. 2010b).

In view of the apparent connection between the AGN's high energy continuum and some IR features, it is of interest to examine this in detail. Although the MIR–X-ray correlation has been extensively studied in the literature (Krabbe, Böker, & Maiolino 2001; Prieto, Pérez García, & Rodríguez Espinosa 2002; Lutz et al. 2004; Ramos Almeida et al. 2007; Horst et al. 2008; Fiore et al. 2009; Gandhi et al. 2009; Levenson et al. 2009; Mason et al. 2012; Sazonov et al. 2012; Matsuta et al. 2012; Ichikawa et al. 2012; Asmus et al. 2015; Mateos et al. 2015; García-Bernete et al. 2016; Ichikawa et al. 2017; Chen et al. 2017), to date there have been no detailed studies using the entire NIR-to-MIR range and selected X-ray bands from 3 to 80 keV. The aim of this work is to investigate this correlation for a sample of 24 nearby unobscured type 1 AGN using new X-ray data obtained with the *Nuclear Spectroscopic Telescope Array* (*NuSTAR*; Harrison et al. 2013) together with archival IR data.

The paper is organized as follows. Section 2 and Section

3 describe the sample selection and the observations, respectively. The X-ray and MIR spectral modelling are presented in Section 4. Section 5 describes the correlation spectrum technique. The main results on the IR to X-ray correlations are presented in Section 6. Finally, in Section 7 we present the discussion and in Section 8 we summarize the main conclusions of this work.

Throughout this paper we assumed a cosmology with $H_0=73\ \text{km s}^{-1}\ \text{Mpc}^{-1}$, $\Omega_m=0.27$, and $\Omega_\Lambda=0.73$, and a velocity-field corrected using the Mould et al. (2000) model, which includes the influence of the Virgo cluster, the Great Attractor, and the Shapley supercluster.

2 SAMPLE SELECTION

The sample studied here consists of 24 unobscured type 1 AGN selected from the *NuSTAR* public archive. The majority of *NuSTAR* observations employed in this work were obtained for detailed broadband spectral analyses published elsewhere (e.g., Ballantyne et al. 2014; Brenneman et al. 2014; Lohfink et al. 2015; Zoghbi et al. 2015; Ursini et al. 2016). These observations are typically long (50–150 ks) and separated into multiple epochs in order to sample spectral variability. The rest of the data were taken as part of the *NuSTAR* survey of *Swift*/BAT-selected AGN, which consists of short observations (15–25 ks) of a large sample representative of the local AGN population (Baloković et al., in preparation). Because of the 100-fold increase in sensitivity between *Swift*/BAT and *NuSTAR*, for any source detected in the *Swift*/BAT all-sky survey, even a short exposure results in data with signal-to-noise ratio (SNR) high enough for spectral modeling up to $\sim 70\ \text{keV}$ (e.g., Baloković et al. 2014; Koss et al. 2015; Masini et al. 2016).

According to the unified model, in type 1 objects we are able to observe the innermost region of the AGN and they are expected to be practically unabsorbed in X-rays. Therefore, we selected all the unobscured type 1 AGN at low redshifts ($z\leq 0.1$) observed with *NuSTAR* and with the X-ray data publicly available in the HEASARC¹ archive. As of April 2016, this sample consists of 67 broad-line AGN. These sources were then cross-correlated with the *Spitzer* Heritage Archive (SHA)² in order to select only those with available *Spitzer/InfraRed Spectrograph* (*IRS*) MIR spectra covering the 5–35 μm range. The final sample used in this paper comprises 24 objects which are listed in Table 1. We note that we have excluded from this work broad-absorption line (BAL) quasars, because their inner region geometry is thought to be significantly different from standard type 1 AGN.

3 OBSERVATIONS

3.1 X-ray *NuSTAR* data

High energy X-ray spectra of the sample studied here were observed with the *NuSTAR* observatory (angular resolution

¹ <http://heasarc.gsfc.nasa.gov/>

² <http://irsa.ipac.caltech.edu/applications/Spitzer/SHA>

Name	Optical type	R.A. (J2000)	Dec. (J2000)	Redshift	Luminosity distance (Mpc)	Spatial scale (pc arcsec ⁻¹)
Mrk 335	Sy 1.2	00h06m19.52s	+20d12m10.5s	0.025	106	490
Fairall 9	Sy 1.2	01h23m45.78s	-58d48m20.8s	0.047	200	885
Mrk 1018	Sy 1.5	02h06m15.99s	-00d17m29.2s	0.042	176	787
Mrk 590	Sy 1.2	02h14m33.56s	-00d46m00.1s	0.026	107	495
Mrk 1044	Sy 1	02h30m05.53s	-08d59m53.3s	0.016	66	311
3C 120	BLRG	04h33m11.10s	+05d21m15.6s	0.032	136	620
Ark 120	Sy 1	05h16m11.42s	-00d08m59.4s	0.032	136	618
1H 0707-495	NLSy 1	07h08m41.50s	-49d33m06.9s	0.041	174	778
RBS 0770	Sy 1.2	09h23m43.00s	+22d54m32.6s	0.033	140	637
NGC 4051	Sy 1.2	12h03m09.61s	+44d31m52.8s	0.003	13	62
NGC 4151	Sy 1.5	12h10m32.58s	+39d24m20.6s	0.005	20	96
PG 1211+143	NLSy 1	12h14m17.67s	+14d03m13.1s	0.083	361	1492
NGC 4593	Sy 1	12h39m39.43s	-05d20m39.3s	0.010	42	198
Mrk 766	Sy 1.5	12h18m26.51s	+29d48m46.3s	0.015	61	289
MCG-06-30-015	Sy 1.2	13h35m53.71s	-34d17m43.9s	0.007	27	128
IC 4329A	Sy 1.2	13h49m19.27s	-30d18m34.0s	0.019	80	372
CGCG 017-073	Sy 1	13h49m52.84s	+02d04m45.1s	0.035	147	666
NGC 5548	Sy 1.5	14h17m59.53s	+25d08m12.4s	0.019	80	375
Mrk 1393	Sy 1.5	15h08m53.95s	-00d11m49.0s	0.056	242	1052
Mrk 290	Sy 1.5	15h35m52.36s	+57d54m09.2s	0.031	130	593
3C 382	BLRG	18h35m03.39s	+32d41m46.8s	0.059	253	1094
3C 390.3	BLRG	18h42m08.99s	+79d46m17.1s	0.057	242	1053
NGC 7213	Sy 1.5	22h09m16.31s	-47d09m59.8s	0.006	25	120
Mrk 915	Sy 1	22h36m46.50s	-12d32m42.6s	0.024	101	468

Table 1. The sample of 24 type 1 AGN studied here sorted by right ascension (R.A.). AGN optical type, R.A. and declination (Dec.) were taken from the NASA/IPAC Extragalactic Database (NED). The redshift, luminosity distance and spatial scale were calculated using a cosmology with $H_0=73 \text{ km s}^{-1} \text{ Mpc}^{-1}$, $\Omega_m=0.27$, $\Omega_\Lambda=0.73$ and a velocity-field corrected using the Mould et al. (2000) model, which includes the influence of the Virgo cluster, the Great Attractor, and the Shapley supercluster.

$\sim 18''$), which consists of two co-aligned hard X-ray telescopes with focal lengths of 10.14 m. *NuSTAR* is the first high energy ($>10 \text{ keV}$) orbiting observatory with focusing optics, providing ~ 2 orders of magnitude increase in sensitivity compared to previous high energy observatories. The data were obtained across the 3–80 keV energy range, using the two *NuSTAR* focal planes: the Focal Plane Module A (FPMA) and the Focal Plane Module B (FPMB), which use CdZnTe chips (pixel size of $2.46''$) and have a field of view (FOV) of $\sim 12' \times 12'$ at 10 keV. A detailed description of the *NuSTAR* observatory is given in Harrison et al. (2013).

We processed the raw *NuSTAR* data using the standard data processing package, NuSTARDAS, generally following the procedures described in the *NuSTAR* user’s guide³ and described in more detail in Baloković et al., in preparation. The complete list of observations is given in Table 2. We used a range of software editions (HEASOFT 6.14–6.16, NuSTARDAS 1.4–1.6) and versions of the calibration database (between 20130909 and 20150316). No significant changes were noted in updating from an older to a newer version of the database for any of our targets. Event filtering was performed using the *nupipeline* script with the most strict filter setting in order to avoid any possible contamination due to South Atlantic Anomaly (SAA) passages and elevated background levels. Sources exhibited a wide range of variability patterns and amplitudes, but in this work we are concerned only with time-averaged data.

³ http://heasarc.gsfc.nasa.gov/docs/nustar/analysis/nustars_wguide.pdf

Name	Obs. ID	Date (UT)	Exp. Time (ks)	F _{3–5 keV}	F _{2–10 keV}	F _{7–15 keV}	F _{15–40 keV}	F _{40–80 keV}
Mrk 335	60001041002	2013/06/13	21.3	$(1.35 \pm 0.72) \times 10^{-12}$	$(4.64 \pm 2.01) \times 10^{-12}$	$(2.98 \pm 0.64) \times 10^{-12}$	$(6.63 \pm 0.65) \times 10^{-12}$	$(4.17 \pm 1.05) \times 10^{-12}$
	60001041003	2013/06/13	21.5					
	60001041005	2013/06/25	92.9					
	80001020002	2014/09/20	68.8					
Mrk 1018	60160087002	2016/02/10	20.3	$(4.91 \pm 0.52) \times 10^{-13}$	$(1.71 \pm 0.11) \times 10^{-12}$	$(1.08 \pm 0.08) \times 10^{-12}$	$(1.62 \pm 0.62) \times 10^{-12}$	$< 5.04 \times 10^{-12}$
Mrk 590	60160095002	2016/02/05	17.9	$(8.89 \pm 0.66) \times 10^{-13}$	$(2.96 \pm 0.14) \times 10^{-12}$	$(1.96 \pm 0.10) \times 10^{-12}$	$(3.48 \pm 0.46) \times 10^{-12}$	$< 1.07 \times 10^{-11}$
Mrk 1044	60160109002	2016/02/08	20.2	$(2.73 \pm 0.10) \times 10^{-12}$	$(8.67 \pm 0.23) \times 10^{-12}$	$(4.19 \pm 0.13) \times 10^{-12}$	$(5.98 \pm 0.47) \times 10^{-12}$	$< 1.50 \times 10^{-11}$
Fairall 9	60001130002	2014/05/09	49.1	$(7.30 \pm 0.05) \times 10^{-12}$	$(2.33 \pm 0.16) \times 10^{-11}$	$(1.24 \pm 0.07) \times 10^{-11}$	$(2.04 \pm 0.07) \times 10^{-11}$	$(1.30 \pm 0.13) \times 10^{-11}$
	60001130003	2014/05/09	93.6					
3C 120	60001042002	2013/02/06	21.6	$(1.60 \pm 0.01) \times 10^{-11}$	$(5.12 \pm 0.11) \times 10^{-11}$	$(2.83 \pm 0.10) \times 10^{-11}$	$(4.57 \pm 0.25) \times 10^{-11}$	$(3.24 \pm 0.09) \times 10^{-11}$
	60001042003	2013/02/06	127.7					
Ark 120	60001044002	2013/02/18	55.3	$(9.99 \pm 3.97) \times 10^{-12}$	$(3.20 \pm 1.19) \times 10^{-11}$	$(1.75 \pm 0.51) \times 10^{-11}$	$(2.97 \pm 0.71) \times 10^{-11}$	$(2.54 \pm 0.11) \times 10^{-11}$
	60001044004	2014/03/22	65.3					
1H 0707-495	60001102002	2014/05/05	144.0	$(1.90 \pm 0.85) \times 10^{-13}$	$(5.50 \pm 2.52) \times 10^{-13}$	$(1.17 \pm 0.48) \times 10^{-13}$	$(5.04 \pm 4.40) \times 10^{-13}$	$< 2.59 \times 10^{-13}$
	60001102004	2014/06/10	48.8					
	60001102006	2014/06/28	46.7					
RBS 0770	60061092002	2012/12/26	18.8	$(6.88 \pm 0.14) \times 10^{-12}$	$(2.20 \pm 0.03) \times 10^{-11}$	$(1.20 \pm 0.02) \times 10^{-11}$	$(1.92 \pm 0.07) \times 10^{-11}$	$(1.14 \pm 0.39) \times 10^{-11}$
NGC 4051	60001050002	2013/06/17	9.4	$(5.79 \pm 2.75) \times 10^{-12}$	$(1.87 \pm 0.82) \times 10^{-11}$	$(1.06 \pm 0.32) \times 10^{-11}$	$(2.18 \pm 0.43) \times 10^{-11}$	$(1.34 \pm 0.25) \times 10^{-11}$
	60001050003	2013/06/17	45.6					
	60001050005	2013/10/09	10.2					
	60001050006	2013/10/09	49.5					
	60001050008	2014/02/16	56.6					
	60001111002	2012/11/12	21.9					
NGC 4151	60001111003	2012/11/12	57.1	$(4.08 \pm 0.59) \times 10^{-11}$	$(1.68 \pm 0.18) \times 10^{-10}$	$(1.58 \pm 0.11) \times 10^{-10}$	$(3.37 \pm 0.18) \times 10^{-10}$	$(2.53 \pm 0.27) \times 10^{-10}$
	60001111005	2012/11/14	61.6					
PG 1211+143	60001100002	2014/02/18	111.2	$(1.31 \pm 0.26) \times 10^{-12}$	$(4.09 \pm 0.80) \times 10^{-12}$	$(1.99 \pm 0.35) \times 10^{-12}$	$(2.99 \pm 0.25) \times 10^{-12}$	$< 5.10 \times 10^{-12}$
	60001100004	2014/04/08	48.8					
	60001100005	2014/04/09	64.3					
	60001100007	2014/07/07	67.2					
NGC 4593	60001149002	2014/12/29	23.3	$(6.37 \pm 1.82) \times 10^{-12}$	$(2.10 \pm 0.58) \times 10^{-11}$	$(1.26 \pm 0.29) \times 10^{-11}$	$(2.41 \pm 0.44) \times 10^{-11}$	$(2.04 \pm 0.28) \times 10^{-11}$
	60001149004	2014/12/31	21.6					
	60001149006	2015/01/02	21.3					
	60001149008	2015/01/04	23.1					
	60001149010	2015/01/06	21.2					
	60001048002	2015/01/24	81.9					
Mrk 766	60001047002	2013/01/29	23.3	$(1.32 \pm 0.32) \times 10^{-11}$	$(4.18 \pm 0.97) \times 10^{-11}$	$(2.31 \pm 0.35) \times 10^{-11}$	$(3.47 \pm 0.33) \times 10^{-11}$	$(1.70 \pm 0.23) \times 10^{-11}$
	60001047003	2013/01/30	127.1					
	60001047005	2013/02/02	29.6					
IC 4329A	60001045002	2012/08/12	159.0	$(3.23 \pm 0.01) \times 10^{-11}$	$(1.07 \pm 0.01) \times 10^{-10}$	$(6.53 \pm 0.02) \times 10^{-11}$	$(1.13 \pm 0.01) \times 10^{-10}$	$(8.61 \pm 0.27) \times 10^{-11}$
CGCG 017-073	60160560002	2015/03/31	15.3	$(1.99 \pm 0.09) \times 10^{-12}$	$(6.80 \pm 0.21) \times 10^{-12}$	$(4.29 \pm 0.15) \times 10^{-12}$	$(8.39 \pm 0.61) \times 10^{-12}$	$< 1.98 \times 10^{-11}$
NGC 5548	60002044002	2013/07/11	24.1	$(9.94 \pm 1.85) \times 10^{-12}$	$(3.50 \pm 0.57) \times 10^{-11}$	$(2.54 \pm 0.27) \times 10^{-11}$	$(4.84 \pm 0.38) \times 10^{-11}$	$(3.82 \pm 0.63) \times 10^{-11}$
	60002044003	2013/07/12	27.2					
	60002044005	2013/07/23	49.4					
	60002044006	2013/09/10	51.4					
	60002044008	2013/12/20	50.0					
	60160607002	2016/01/19	21.5					
Mrk 290	60061266002	2013/11/14	25.0	$(2.25 \pm 0.17) \times 10^{-12}$	$(7.54 \pm 0.38) \times 10^{-12}$	$(4.80 \pm 0.07) \times 10^{-12}$	$(9.30 \pm 0.69) \times 10^{-12}$	$< 2.43 \times 10^{-11}$
	60061266004	2013/11/27	26.3					
3C 382	60061286002	2012/09/18	16.6	$(1.19 \pm 0.47) \times 10^{-11}$	$(3.94 \pm 1.47) \times 10^{-11}$	$(2.30 \pm 0.75) \times 10^{-11}$	$(3.51 \pm 0.05) \times 10^{-11}$	$(2.26 \pm 0.12) \times 10^{-11}$
	60001084002	2013/12/18	82.4					
3C 390.3	60001082002	2013/05/24	23.6	$(1.26 \pm 0.01) \times 10^{-11}$	$(4.20 \pm 0.03) \times 10^{-11}$	$(2.52 \pm 0.01) \times 10^{-11}$	$(3.97 \pm 0.05) \times 10^{-11}$	$(2.96 \pm 0.04) \times 10^{-11}$
	60001082003	2013/05/24	47.5					
NGC 7213	60001031002	2014/10/05	101.5	$(4.90 \pm 0.05) \times 10^{-12}$	$(1.60 \pm 0.01) \times 10^{-11}$	$(8.66 \pm 0.07) \times 10^{-12}$	$(1.20 \pm 0.02) \times 10^{-11}$	$(7.64 \pm 1.19) \times 10^{-12}$
Mrk 915	60002060002	2014/12/02	52.9	$(1.72 \pm 0.69) \times 10^{-12}$	$(5.95 \pm 2.33) \times 10^{-12}$	$(4.25 \pm 1.35) \times 10^{-12}$	$(7.52 \pm 2.48) \times 10^{-12}$	$(6.49 \pm 2.80) \times 10^{-12}$
	60002060004	2014/12/07	54.1					
	60002060006	2014/12/12	50.6					

Table 2. Summary of the X-ray observations. Columns 1 to 4 list the object name, the observation ID, the observation date and the exposure time. Columns 5 to 9 correspond to the 3-5, 2-10, 7-15, 15-40 and 40-80 keV band fluxes, respectively. The X-ray fluxes were calculated by averaging all the observations available (the fluxes are given in $\text{erg s}^{-1} \text{cm}^{-2}$ units). We note that for the individual observations the uncertainties correspond to 1σ level, whereas for multiple observations the uncertainties correspond to the standard deviation between the different observations, which are larger than the propagated uncertainties.

We extracted target spectra from circular regions centered on the source in each of the two focal plane modules (FPMA and FPMB), with the radii size chosen according to the total number of counts, between 30'' and 150''. The different sizes used here depend on the brightness of the source. For the faintest objects we used a 30'' aperture, whereas for the brightest ones we used larger apertures to collect more photons since the background is low in those cases. The background extraction region is defined as the square area of the detector onto which the target is focused, excluding the circular region 30% larger than the source extraction region and excluding 30'' around any detected serendipitous sources (see Lansbury et al. 2017). With its spatial resolution of $\sim 28''$ (half-power diameter; Harrison et al. 2013), *NuSTAR* cannot spatially resolve any of our targets. The source and background spectra were produced together with the ancillary response files using the *nuproducts* script. The spectral files were grouped into energy bins so that the median SNR is 5–15 in each bin (depending on the total number of counts), with a minimum SNR of 5 for most sources and 3 for the faintest ones.

3.2 MIR Spitzer Space Telescope spectra

We retrieved MIR spectra for the whole sample from the Cornell Atlas of *Spitzer/IRS* Source (CASSIS⁴ v4; Lebouteiller et al. 2011). The spectra were obtained using the IRS instrument (Houck et al. 2004). The bulk of the observations (18/24 galaxies) were made in staring mode using the low-resolution (R \sim 60–120) IRS modules: the short-low (SL; 5.2–14.5 μm) and the long-low (LL; 14–38 μm). The spectra were reduced with the CASSIS software, using the optimal extraction to obtain the best SNR. We only needed to apply a small offset to stitch together the different modules, taking the shorter wavelength module (SL2; 5.2–7.6 μm) as the basis, which has associated a slit width of 3.6''.

We note that for six galaxies (Mrk 335, Mrk 1044, 1H 0707–495, NGC 4151, NGC 4593, and Mrk 766) there are no low-resolution staring mode spectra for the LL module. Therefore, in order to cover the same spectral range, we used the SL low-resolution module together with the high-resolution (HR; R \sim 600) IRS modules: the short-high (SH; 9.9–19.6 μm) and the long-high (LH; 18.7–37.2 μm) available in the CASSIS. The high-resolution module spectra are also reduced with the CASSIS software, using the optimal extraction. We have consistently applied a Gaussian convolution in the HR spectra to degrade the spectral resolution to be the same as that for the low-resolution spectra. The MIR spectra are shown in Appendix A. Further details on the *Spitzer* observations can be found in Table 3.

As a sanity check, and since we are interested only in AGN-dominated IR data, we estimated the possible contribution from other components to the IRS spectra of our sample. To do so, we used the *DeblendIRS*⁵ routine (Hernán-Caballero et al. 2015), that decomposes MIR spectra using a linear combination of three spectral components: AGN, PAH and stellar emission. We found that the MIR

spectra of the galaxies in our sample have a high contribution of the AGN ($\sim 90\%$; i.e. AGN-dominated systems), as expected for type 1 AGN. Further details on the spectral decomposition can be found in Appendix A.

3.3 NIR data

In order to complete our IR–X-ray correlation analysis we extended our collection of data to include NIR fluxes. To achieve this we compiled cross-dispersed NIR spectra for roughly half of our sample (15/24 sources; see Table 2), obtained either with the SpeX spectrograph (Rayner et al. 2003) on the 3.0 m NASA Infrared Telescope Facility (IRTF) or with the Gemini Near-Infrared Spectrograph (GNIRS) on the 8.1 m Gemini-North Telescope. These spectra are presented in Rodríguez-Ardila et al. (2002); Riffel, Rodríguez-Ardila, & Pastoriza (2006); Landt et al. (2008, 2011, 2013); Lamperti et al. (2017) and Landt et al., in preparation. We used the Galactic extinction corrected NIR spectra to derive rest-frame *J*- and *K*-band fluxes measured in a small aperture.

Finally, for the rest of the sample, we retrieved lower angular resolution *J*- and *K*-band photometry from the Two Micron All-Sky Survey (2MASS; Skrutskie et al. 2006) Point Source Catalog⁶, which were obtained with 1.3 m telescopes. These fluxes were extracted with the 2MASS point source processing software, using an aperture radius of 4''. Further details on the NIR observations can be found in Table 3.

4 SPECTRAL MODELLING

4.1 X-ray modelling

We performed spectral analysis in *Xspec* (Arnaud 1996), version 12.8.2. We analysed each observation separately, and fitted spectra from FPMA and FPMB modules simultaneously without coadding. A cross-normalization factor was employed to account for small relative offsets between FPMA and FPMB. In all cases it was found to be consistent with expectations from calibration, typically $< 5\%$ (Madsen et al. 2015). In this work we are only dealing with photometry within the various X-ray bands, and so we did not attempt to separate out different spectral components. Instead, we performed spectrophotometry in the 3–5, 7–15, 15–40, and 40–80 keV bands. These bands were chosen to avoid the Fe $K\alpha$ and sample the continuum and the Compton hump. For each of the bands separately, we assumed a simple power-law model, which provided a satisfactory fit in nearly all cases. For spectra with very high data quality, some of these fits resulted in χ^2 greater than 1.5. In those cases we also fitted the data with a log-parabolic model (*logpar* in *Xspec*), which provided a better fit and did not result in a significantly different band flux. We calculated band fluxes and their statistical uncertainties (defined as 68% confidence intervals) from these fits based on χ^2 statistics, which are shown in Table 2. These fluxes are corrected for the generally low Galactic column density taken from Dickey & Lockman 1990.

For approximately 40% of our sample, the data in the

⁴ <http://cassis.astro.cornell.edu/atlas/>

⁵ <http://www.denebola.org/ahc/deblendIRS/>

⁶ <http://www.ipac.caltech.edu/2mass/releases/allsky/>

Name	MIR data			NIR data		Ref.
	Telesc./Instr.	Obs. ID	Date (UT)	Telesc./Instr. or database	Date (UT)	
Mrk 335	<i>Spitzer/IRS</i> L	14448128-1	08 Jul 2005	IRTF/SpeX	25 Jan 2007	a
	<i>Spitzer/IRS</i> H	14448128-2	12 Jan 2009	
Fairall 9	<i>Spitzer/IRS</i> L	28720896	20 Jan 2009	2MASS	21 Oct 1999	b
Mrk 1018	<i>Spitzer/IRS</i> L	15076096	28 Jan 2006	Gemini/GNIRS	16 Nov 2012	c
Mrk 590	<i>Spitzer/IRS</i> L	18508544	09 Feb 2007	IRTF/SpeX	24 Jan 2007	a
Mrk 1044	<i>Spitzer/IRS</i> L/H	14447872	04 Aug 2005	IRTF/SpeX	11 Oct 2000	d
3C 120	<i>Spitzer/IRS</i> L	18505216	06 Oct 2007	Gemini/GNIRS	15 Dec 2010	e
Ark 120	<i>Spitzer/IRS</i> L	18941440	05 Oct 2005	IRTF/SpeX	26 Jan 2007	a
1H 0707-495	<i>Spitzer/IRS</i> L/H	14447360	15 Nov 2006	2MASS	26 Feb 2000	b
RBS 0770	<i>Spitzer/IRS</i> L	2691392	08 Dec 2004	2MASS	30 Nov 2000	b
NGC 4051	<i>Spitzer/IRS</i> L	14449152	10 Dec 2005	IRTF/SpeX	20 Apr 2002	f
	<i>Spitzer/IRS</i> H	10342400	01 Jun 2005	
NGC 4151	<i>Spitzer/IRS</i> L	3754496	08 Jan 2004	IRTF/SpeX	08 Jan 2006	g
PG 1211+143	<i>Spitzer/IRS</i> L	3760896	07 Jan 2004	Gemini/GNIRS	18 Dec 2011	e
NGC 4593	<i>Spitzer/IRS</i> L/H	4853504	01 Jul 2005	IRTF/SpeX	11 Jun 2006	g
Mrk 766	<i>Spitzer/IRS</i> L/H	14448896	22 Jun 2006	IRTF/SpeX	21 Apr 2002	f
MCG-06-30-015	<i>Spitzer/IRS</i> L	4849920	28 Jun 2004	2MASS	06 Apr 1991	b
IC 4329A	<i>Spitzer/IRS</i> L	18506496	29 Jul 2007	2MASS	25 Jul 1998	b
CGCG 017-073	<i>Spitzer/IRS</i> L	26497024	05 Aug 2008	2MASS	28 Feb 2000	b
NGC 5548	<i>Spitzer/IRS</i> L	18513152	31 Jul 2007	IRTF/SpeX	12 Jun 2006	g
Mrk 1393	<i>Spitzer/IRS</i> L	15080960	13 Aug 2005	2MASS	11 Mar 1999	b
Mrk 290	<i>Spitzer/IRS</i> L	14200320	22 Dec 2005	IRTF/SpeX	11 Jun 2006	g
3C 382	<i>Spitzer/IRS</i> L	11306496	15 Aug 2005	2MASS	25 Jan 1998	b
3C 390.3	<i>Spitzer/IRS</i> L	4673024	24 Mar 2004	Gemini/GNIRS	04 Aug 2011	e
NGC 7213	<i>Spitzer/IRS</i> L	18513152	31 Jul 2007	2MASS	18 Nov 1998	b
Mrk 915	<i>Spitzer/IRS</i> L	26495488	29 Jun 2008	IRTF/SpeX	15 Sep 2011	h

Table 3. Summary of the IR observations. The columns are as follows: (1) object name. For the MIR data (2) telescope, instrument and grating, where L and H correspond to the low- and high-resolution modules, respectively; (3) observation ID; and (4) observation date. For the NIR data (5) telescope and instrument; (6) observation date; and (7) corresponding references. References: a) Landt et al. (2011); b) Skrutskie et al. (2006); c) Landt et al., in preparation; d) Rodríguez-Ardila et al. (2002); e) Landt et al. (2013); f) Riffel, Rodríguez-Ardila, & Pastoriza (2006); g) Landt et al. (2008); h) Lamperti et al. (2017).

40-80 keV band is of insufficient quality to yield a robust flux measurement, i.e., there are too few source counts for performing the fit described above. In such cases, we extend the band toward lower energies (down to 30 keV, or 20 keV for the faintest sources) and fix the photon index to 2.0 in order to estimate the 40-80 keV flux. We adopt the upper end of the 68% confidence interval of these estimates as 1σ upper limits and, then, we calculated 3σ upper limits which are employed in this study (see Table 2). For completeness and comparison with the literature, we also computed fluxes in the 2-10 keV band using *NuSTAR* data in the 3-5 and 7-15 keV bands, hence avoiding any flux contributed by the neutral Fe $K\alpha$ line detected in many sources in our sample. Fluxes averaged over multiple observation epochs are given in Table 2.

4.2 MIR modelling

We used the PAHFIT v1.2 routine (Smith et al. 2007) to fit the MIR continuum and the dust emission features of the IRS spectra. The purpose of these fits is to obtain emission-line spectra for all the galaxies. To do so, we used the default model continuum dust temperatures (300, 200, 135, 90, 65, 50, 40 and 35 K) and a stellar continuum component. Fig. 1 shows two examples of these fits.

Once we subtracted the continuum emission and the

dust emission features contribution to each MIR spectrum, we obtain the emission-line spectrum for each galaxy. To measure the integrated emission line fluxes we used the DIPSO⁷ (Howarth et al. 2004) Emission-Line Fitting routine. Single Gaussians were sufficient to reproduce the line profiles.

In Table 4 we list the integrated fluxes of the MIR emission lines used in this study, which are [SIV] λ 10.51, [Ne II] λ 12.81, [Ne V] λ 14.32, [Ne III] λ 15.56, [S III] λ 18.71, [O IV] λ 25.89 and [Si II] λ 34.82 (all wavelengths given in μ m). In the case of the three galaxies for which particular emission lines are not detected we calculated 3σ upper limits (see Table 4).

⁷ DIPSO is a Starlink package to analyse spectra.

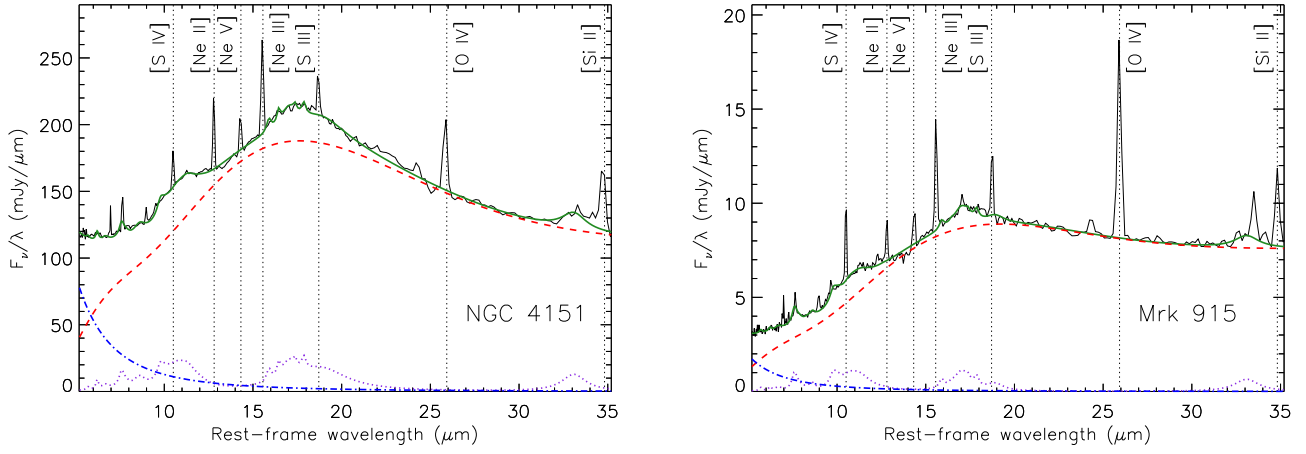


Figure 1. Examples of the MIR spectral modelling using PAHFIT. We show the *Spitzer/IRS* rest-frame spectra (black solid lines), model fits (green solid lines), dust continuum (red dashed lines), dust emission features (purple dotted lines) and stellar continuum (blue dot-dashed lines). The black vertical dotted lines correspond to the MIR emission lines used in this study.

Object	[SIV] λ 10.51	[Ne II] λ 12.81	[Ne V] λ 14.32	[Ne III] λ 15.56	[S III] λ 18.71	[O IV] λ 25.89	[Si II] λ 34.82	J-band	K-band	6 μ m	12 μ m	18 μ m
Mrk 335	25.5 \pm 1.8	16.6 \pm 1.2	10.5 \pm 0.2	25.0 \pm 0.7	64.4 \pm 2.8	72.9 \pm 1.5	78.2 \pm 6.6	192.0	347.6	512.2	479.7	441.1
Fairall 9	50.3 \pm 7.5	33.3 \pm 4.6	21.5 \pm 6.6	62.8 \pm 10.1	18.8 \pm 2.8	70.1 \pm 6.5	23.5 \pm 6.5	231.7	332.7	806.1	748.2	717.5
Mrk 1018	9.3 \pm 1.2	8.9 \pm 1.3	3.4 \pm 1.4	17.7 \pm 2.4	12.6 \pm 2.1	24.6 \pm 2.7	15.2 \pm 2.3	91.0	84.8	182.0	141.9	128.9
Mrk 590	20.8 \pm 5.1	27.4 \pm 1.1	7.4 \pm 3.1	31.2 \pm 4.2	10.9 \pm 1.7	32.9 \pm 2.5	29.4 \pm 9.5	359.8	291.9	112.4	234.0	309.1
Mrk 1044	19.3 \pm 3.4	45.7 \pm 1.6	22.0 \pm 0.3	28.5 \pm 0.6	16.5 \pm 0.7	16.4 \pm 0.3	65.4 \pm 3.1	136.7	272.3	304.0	270.5	237.5
3C 120	202.7 \pm 9.7	49.9 \pm 4.1	173.3 \pm 11.3	268.3 \pm 9.2	50.7 \pm 13.0	875.5 \pm 21.5	142.0 \pm 16.2	178.7	383.2	528.2	640.8	759.2
Ark 120	44.5 \pm 15.5	26.3 \pm 4.0	15.7 \pm 1.4	37.1 \pm 5.4	14.5 \pm 3.1	60.6 \pm 6.6	33.2 \pm 8.4	717.5	1053.8	798.8	627.0	525.0
1H 0707-495	6.3 \pm 0.9	3.8 \pm 0.2	5.0 \pm 0.1	21.3 \pm 0.6	<5.5	21.1 \pm 1.0	32.2 \pm 3.3	64.4	74.4	57.1	65.1	70.0
RBS 0770	36.5 \pm 7.4	25.0 \pm 1.9	23.4 \pm 2.0	70.1 \pm 2.3	20.5 \pm 1.7	70.8 \pm 3.4	40.0 \pm 5.4	240.1	271.4	261.5	289.9	308.3
NGC 4051	46.3 \pm 17.6	198.5 \pm 5.1	126.4 \pm 5.0	214.2 \pm 1.9	107.5 \pm 4.0	354.0 \pm 3.6	122.2 \pm 6.6	430.8	559.4	645.9	1259.2	1415.6
NGC 4151	957.9 \pm 33.7	1606.3 \pm 42.8	796.1 \pm 58.3	2352.0 \pm 50.6	854.73 \pm 61.5	1990.0 \pm 101.4	1404.6 \pm 192.1	1084.2	1683.4	3503.0	4916.4	6410.4
PG 1211+143	<32.3	6.2 \pm 0.6	4.2 \pm 0.6	11.9 \pm 1.9	<9.6	9.8 \pm 3.0	<22.7	127.0	202.9	391.9	402.4	403.4
NGC 4593	33.3 \pm 17.5	61.2 \pm 3.9	77.3 \pm 3.1	115.9 \pm 3.7	50.8 \pm 0.7	112.2 \pm 2.2	102.1 \pm 3.1	393.5	707.3	971.9	846.4	841.1
Mrk 766	93.4 \pm 30.3	225.4 \pm 10.7	229.7 \pm 2.0	290.0 \pm 2.2	125.6 \pm 4.0	454.5 \pm 1.5	114.6 \pm 3.9	285.0	517.3	502.7	825.2	1332.4
MCG-06-30-015	85.6 \pm 13.6	48.0 \pm 7.0	40.9 \pm 11.4	60.0 \pm 4.4	56.6 \pm 5.8	140.4 \pm 14.6	31.9 \pm 5.9	506.8	711.4	499.9	596.8	675.6
IC 4329A	384.4 \pm 45.0	234.8 \pm 14.3	351.1 \pm 19.9	611.6 \pm 37.6	225.4 \pm 29.3	993.4 \pm 44.2	434.9 \pm 46.3	1159.9	1749.4	2561.7	2672.8	2868.2
CGCG 017-073	12.5 \pm 1.1	9.1 \pm 1.8	14.0 \pm 4.4	20.1 \pm 2.0	43.0 \pm 1.7	42.3 \pm 1.4	18.4 \pm 3.1	131.6	163.6	74.1	89.5	99.9
NGC 5548	59.1 \pm 3.4	88.5 \pm 3.9	33.4 \pm 9.1	93.0 \pm 7.4	43.2 \pm 5.5	89.1 \pm 15.5	97.8 \pm 24.5	277.6	364.4	321.1	508.2	652.4
Mrk 1393	37.8 \pm 1.2	15.5 \pm 1.1	28.0 \pm 2.3	63.5 \pm 5.2	21.7 \pm 1.8	116.5 \pm 3.2	13.3 \pm 3.6	101.6	97.1	64.5	88.7	140.1
Mrk 290	24.1 \pm 1.5	23.0 \pm 1.2	20.9 \pm 2.7	42.5 \pm 2.3	17.7 \pm 4.4	56.6 \pm 5.1	11.9 \pm 3.8	167.5	233.2	173.5	225.7	272.3
3C 382	11.9 \pm 1.0	10.6 \pm 1.2	7.3 \pm 0.4	19.9 \pm 3.4	8.8 \pm 1.3	18.2 \pm 1.6	19.1 \pm 2.2	407.8	497.2	404.8	226.1	182.6
3C 390.3	10.3 \pm 2.2	35.3 \pm 1.3	7.6 \pm 2.2	31.4 \pm 2.4	8.5 \pm 0.7	31.8 \pm 3.3	18.4 \pm 2.9	153.9	262.1	252.4	295.3	346.9
NGC 7213	<225.3	258.0 \pm 6.1	10.4 \pm 2.0	162.0 \pm 7.7	26.4 \pm 7.8	18.0 \pm 1.5	138.4 \pm 14.3	1677.1	1486.3	456.1	668.6	680.3
Mrk 915	137.4 \pm 4.6	58.6 \pm 4.7	68.8 \pm 11.3	170.8 \pm 2.9	82.1 \pm 5.2	344.1 \pm 4.5	96.9 \pm 8.1	160.6	196.3	102.8	205.1	292.9

Table 4. MIR emission line fluxes (in 10^{-15} erg s $^{-1}$ cm $^{-2}$ units) and J -, K -, N - and Q -band fluxes (in 10^{-13} erg s $^{-1}$ cm $^{-2}$ units) employed here. The estimated uncertainties for the J - and K -band (1.2 and 2.2 μ m), and MIR bands (6, 12 and 18 μ m) are \sim 10% and \sim 20%, respectively.

5 THE CORRELATION SPECTRUM TECHNIQUE (CST)

As explained in Section 1, hard X-rays are good tracers of the AGN power due to the high energies involved in the accretion process. On the other hand, dust in the central region of AGN reprocesses some fraction of these high-energy photons, which are then re-emitted in the IR. For this reason the MIR–X-ray correlation has been widely studied for different types of AGN at various MIR wavelengths (~ 6 to $25 \mu\text{m}$; see García-Bernete et al. 2016 and references therein). However, to date there have been no detailed studies across the entire IR spectral range, and in relation to a set of X-ray bands defined from 3 to 80 keV. In order to do this we employ a new technique which can be used to determine the IR wavelength at which the correlation peaks and to identify specific features closely linked to the AGN.

Here we present the IR to X-ray correlation spectrum (hereafter IRXCS) for our sample of 24 type 1 AGN. We used the correlation spectrum technique (CST), developed for medium to large samples of objects by Jin, Ward, & Done (2012). This technique consists of cross-correlating the monochromatic luminosities at each wavelength of the entire rest-frame spectrum with a given X-ray band for a sample of sources. First, we used the *Spitzer/IRS* MIR spectral range (~ 5 – $35 \mu\text{m}$) and calculated the monochromatic luminosity at ~ 1000 wavelengths evenly distributed throughout it. Then we used the Spearman’s rank test to evaluate the correlation coefficients at each of these monochromatic MIR luminosities with all the X-ray bands considered here, resulting in the IRXCS for each band. We then plot the correlation coefficients for the 2–10, 7–15, 15–40 and 40–80 keV bands⁸ against wavelength as brown solid lines in Fig. 2. The diagnostic power of this method is that it can reveal how a general correlation between a spectral range, in this case the IR, changes across it. We refer the reader to Jin, Ward, & Done (2012) for further details on the CST technique.

In addition to the MIR correlation spectra, in Fig. 2 we included the NIR correlation coefficients (*J*- and *K*-bands; black asterisks) to increase the IR spectral coverage, and also those measured for the MIR emission lines (purple circles). Finally, we list the IPs of the MIR emission lines (black vertical dotted lines), the PAH and silicate features (orange and blue vertical solid lines), and the maximum of each IRXCS (grey vertical region).

The correlation coefficients plotted in Fig. 2 were calculated taking into account the upper limits to the MIR emission line luminosities (see Table 4) and also to the 40–80 keV band luminosities (see Table 2). In order to do that, the correlations were carried out with the ASURV survival analysis package (Feigelson & Nelson 1985; Isobe, Feigelson, & Nelson 1986) using the Spearman’s rank test and the Buckley-James method for censored data.

To test the survival analysis we first repeated the correlations for the emission lines without including the upper limits. As expected, we found practically the same results because there are few upper limits (only three galaxies and five upper limits in total). In contrast, the correlation spec-

trum when we do not consider the upper limits to the 40–80 keV band luminosities is significantly different. This indicates that in this case the number of upper limits is too large (40% of the sample) to yield a robust IRXCS.

We then produced a new version of Fig. 2 for the 15 sources without upper limits in the 40–80 keV band (see Appendix B). We found the same correlation strengths and shape for all the X-ray energy bands, confirming that the lower correlation coefficients shown for the 40–80 keV band IRXCS in the bottom-right panel of Fig. 2 are just a consequence of including a large number of upper limits and so do not correspond to any real trend. Therefore in the following we will only consider the results for the 3–5, 2–10, 7–15 and 15–40 keV bands, although we note that the spectral shape of the 40–80 keV IRXCS is the same as those of the lower energy bands.

Finally, we note that the luminosity-luminosity correlations might be caused, at least in part, by distance effects. Therefore, we also checked the same correlations in flux-flux space. The correlations using the luminosities are stronger than the flux-flux correlations, but the latter are still significant and show practically the same trends.

6 THE IRXCS OF TYPE 1 AGN

From the analysis performed here, we find that all the hard X-ray bands correlate well with the entire IR spectrum, with the correlation maximum being around ~ 15 – $20 \mu\text{m}$ (see Fig. 2). In general the correlation spectra are smooth, although they show some features. In the MIR, the most prominent are the silicate band at ~ 10 – $10.5 \mu\text{m}$, the ~ 33 – $34 \mu\text{m}$ crystalline silicate broad plateau (e.g., Sturm et al. 2000; Smith et al. 2007) and various MIR emission lines. See Section 7 for discussion of the implications of these findings.

In the NIR, we find a stronger correlation for the *K*-band than for the *J*-band. While the *J*-band data follows the trend of the bluest part of the MIR correlation (correlation coefficient ~ 0.80), the *K*-band data correlates with the X-rays at a similar level as found for the $10 \mu\text{m}$ emission ($\rho \sim 0.85$). The result is a correlation peak at $\sim 2 \mu\text{m}$. Although for the NIR data we have not confirmed that all the fluxes are AGN-dominated, as we did for the MIR spectra (see Appendix A), the apertures used to extract the NIR fluxes are similar or smaller than the IRS aperture. Therefore we are confident that for the majority of the galaxies the NIR fluxes are indeed AGN-dominated. Note that we find a less significant correlation for the *K*-band luminosities ($\rho \sim 0.77$) and no changes for the *J*-band luminosities by using the lower angular resolution 2MASS fluxes for all the sample. This indicates that by using higher angular resolution fluxes we can recover AGN-dominated fluxes in the *K*-band, but not in the *J*-band, where the host galaxy emission is much higher, as claimed by Kotilainen et al. (1992). These authors found that the non-stellar fraction generally increases towards longer NIR wavelengths in a complete hard X-ray selected sample of AGN (mainly type 1). Indeed, they found that for the majority of the sources in their sample the *K*-band continuum from an aperture of $3''$ diameter is dominated by non-stellar emission.

By comparing the results for the 3–5, 2–10, 7–15 and 15–40 keV bands, we observe that the correlation coefficients de-

⁸ Note that we do not show the 3–5 keV IRXCS in the Fig. 2 since this X-ray band is included in the 2–10 keV band and the resulting correlation spectra are practically identical.

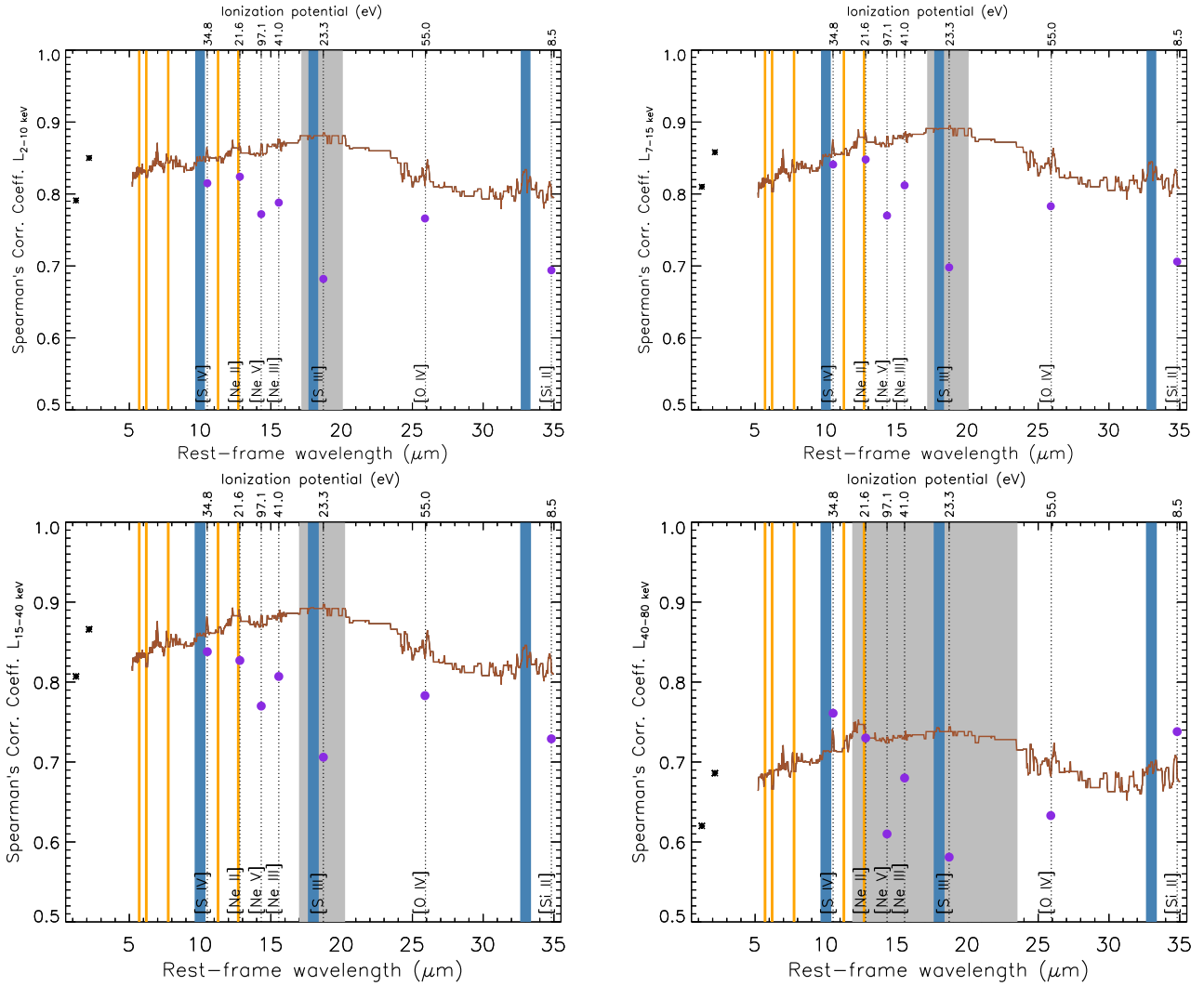


Figure 2. Correlation spectra of the sample of 24 type 1 AGN studied here. From top left to bottom right panels: 2-10, 7-15, 15-40 and 40-80 keV bands. We show the rest-frame IRXCS (brown solid line), the NIR (black asterisks) and the MIR emission line correlation coefficients (purple circles). The orange and blue vertical solid lines correspond to PAH and silicate features, respectively, and the black vertical dotted lines are the MIR emission lines. The grey vertical region identifies the maximum of the correlation.

rived here are practically identical (see left panel of Fig. 3). The correlation coefficients are ~ 0.87 - 0.88 at $20 \mu\text{m}$, ~ 0.85 - 0.86 at 2.2 and $10 \mu\text{m}$, and ~ 0.80 at 1.2 and $30 \mu\text{m}$.

We also performed linear regressions for the commonly used 2-10 keV X-ray band in log-log space using the Buckley-James least squares method (see Feigelson & Nelson 1985 and Isobe, Feigelson, & Nelson 1986 for further details) to compare with previous studies. In Fig. 4 we show these linear regressions using three monochromatic luminosities measured from the MIR spectra (6 , 12 and $18 \mu\text{m}$). We find tight correlations for the three MIR luminosities considered ($\rho = 0.83$, 0.86 and 0.88 , respectively; see Fig. 4). This is in agreement with the results reported by Asmus et al. (2015) using the same X-ray band and high angular resolution MIR data at 12 and $18 \mu\text{m}$ for samples of 152 and 38 AGN, respectively. On the other hand, using lower angular resolution MIR data from the *Infrared Imaging Satellite* “AKARI”, Matsuta et al. (2012) reported a higher correlation signifi-

cance between the 14–195 keV and $9 \mu\text{m}$ luminosities than for those at $18 \mu\text{m}$ for a large sample of type 1 AGN.

The slopes that we measure for the MIR–2-10 keV correlations are ~ 1 (see Fig. 4), in agreement with previous studies using the same X-ray band and similar MIR wavelengths (~ 6 to $25 \mu\text{m}$; see García-Bernete et al. 2016 and references therein). For example, using data from *ISO-CAM* and the *Wide-field Infrared Survey Explorer* (*WISE*) at $\sim 6 \mu\text{m}$, Ramos Almeida et al. (2007) and Mateos et al. (2015) found slopes of ~ 1.0 and ~ 1.1 for type 1 AGN respectively. On the other hand, Fiore et al. (2009) reported a flatter slope of ~ 0.7 by using $5.8 \mu\text{m}$ fluxes of type 1 AGN from the *Spitzer/Infrared Array Camera* (*IRAC*) with $\log L_{(5.8 \mu\text{m})} > 43.04$. Using high angular resolution $12 \mu\text{m}$ fluxes from VISIR, Gandhi et al. (2009) found a slope of ~ 1.2 for a sample of type 1 AGN.

We also find identical slopes (1.12) at 12 and $18 \mu\text{m}$ (see central and right panels of Fig. 4), which is in agreement with the results reported by Asmus et al. (2015) and

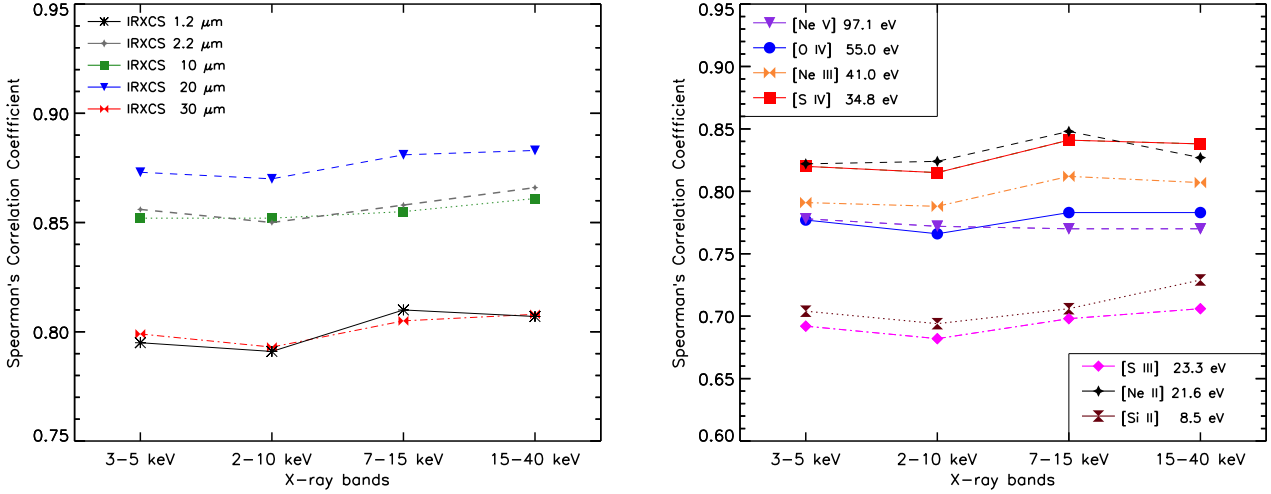


Figure 3. Comparison between the different correlation coefficients for each X-ray band. Left panel: Correlation coefficients at different continuum wavelengths (1.2, 2.2, 10, 20 and 30 μm). Right panel: same as in the left panel, but for the MIR emission lines.

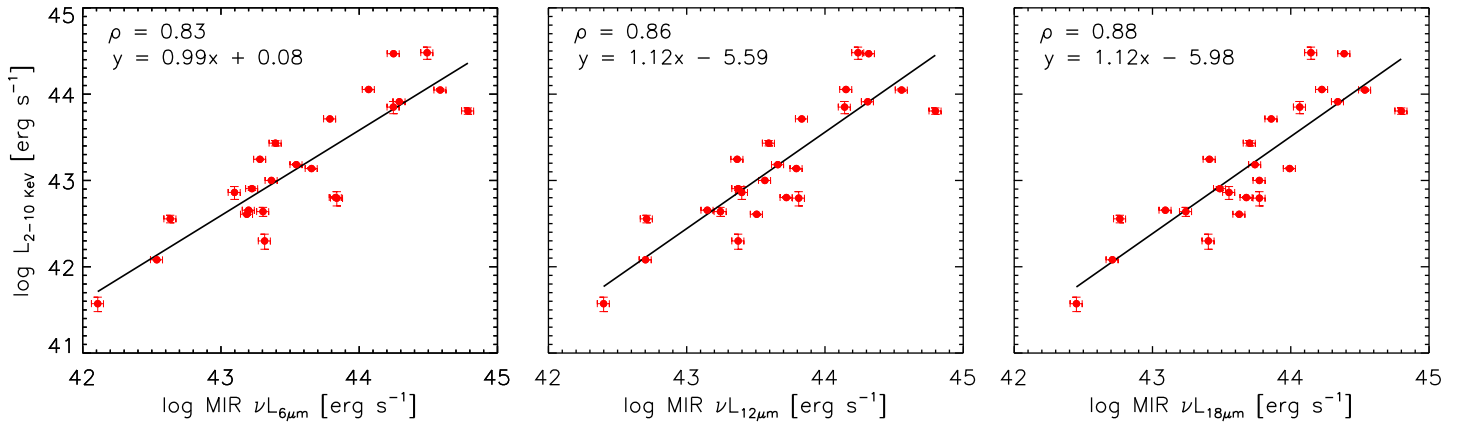


Figure 4. MIR–2–10 keV X-ray luminosity correlations (using 6, 12 and 18 μm luminosities). The vertical error bars correspond to the 2–10 keV uncertainties listed in Table 2. The horizontal error bars correspond to the estimated uncertainty of the MIR fluxes, which is ~20% for the *Spitzer* spectra.

Ichikawa et al. (2017). Asmus et al. (2015) found slopes of ~1.0 by using high angular resolution fluxes at 12 and 18 μm for large samples of AGN, and Ichikawa et al. (2017) reported the same slopes for the 12 μm–14–195 keV and 22 μm–14–195 keV correlations (1.04 and 1.02 respectively) using low angular resolution MIR data of a large sample of AGN.

Regarding the MIR emission lines (shown as purple circles in Fig. 2), we do not find a clear correlation between IP and the correlation strength. This is shown in the right panel of Fig. 3. All the lines considered here show correlation coefficients ≥ 0.7 . It is worth noting the strong correlation between the low IP [Ne II] line and the X-rays ($\rho \sim 0.83$). The strength of the correlation is practically the same for the [Ne II] and [S IV] lines, closely followed by [Ne III], [O IV] and [Ne V]. Finally, the lower correlation coefficients are those of [S III] and [Si II].

As for the IR continuum, the emission line correlation

coefficients are practically constant in the four X-ray bands considered (see right panel of Fig. 3).

7 DISCUSSION

As explained in Section 2, unobscured type 1 AGN are ideal laboratories for studies of the emission from, and components within, the nuclear region. Indeed we confirm that the MIR spectra of our sample galaxies are AGN-dominated (~90% of AGN contribution; see Appendix A). This result, together with the tightness of the correlations between the hard X-rays and the entire NIR-to-MIR range (see Fig. 2) confirms that the IR emission of our sample is AGN-dominated.

The correlation method applied here allows us to examine how the IR versus X-ray correlations change across the entire IR spectral coverage (~1–35 μm). The IRXCS for various hard X-ray energy bands between 3 and 40 keV shows a

correlation maximum at $\sim 15\text{--}20\ \mu\text{m}$ (see Fig. 2). This correlation peak coincides with the maximum AGN contribution to the MIR spectra for the majority of the sources analyzed here (see Appendix A). At $\lambda \gtrsim 20\ \mu\text{m}$ the correlation spectrum slowly decreases.

Although the spectral shape of the IRXCS are relatively smooth, there are some specific features. An example is the silicate feature, which for our sample peaks at $\sim 10\text{--}10.5\ \mu\text{m}$ (see Fig. 2 and Appendix A), as generally found for type 1 AGN (Hao et al. 2005; Landt, Buchanan, & Barmby 2010; Hatziminaoglou et al. 2015). Another feature in the correlation spectrum is the $\sim 33\text{--}34\ \mu\text{m}$ broad plateau (e.g., Sturm et al. 2000; Smith et al. 2007). This feature is generally attributed to crystalline silicates such as olivines and it has also been detected in the MIR spectra of comets and planetary nebulae (Koike, Shibai, & Tuchiyama 1993; Waters et al. 1998). The significant correlation of this emission feature with the hard X-rays indicates that it is produced by dust heated by the AGN. A further investigation on the influence of spectral features would be to check whether the PAH features, which are primarily related to star formation, show a de-correlation. However, the galaxies in our sample show weak or absent PAH lines (fractional contribution $< 10\%$ according to our spectral decomposition analysis; see Table A1), preventing us from performing this test. From Fig. 2 it seems that the $6.2\ \mu\text{m}$ band is de-correlated with the X-rays, but the others are not. A sample of AGN with strong PAHs is needed to confirm this de-correlation. Another interesting result is that we observe a tendency in the different IR features detected in the IRXCS to be more prominent when they are far from the correlation maximum. This could be the result of dilution of the features where the AGN continuum contribution is at its maximum.

In the NIR we see the correlation peak at $\sim 2\ \mu\text{m}$, as the K-band emission is more strongly correlated with the X-rays than the J-band emission. This could be related to the NIR bump observed in the spectral energy distributions (SEDs) of some type 1 AGN ($\sim 1\text{--}5\ \mu\text{m}$; Mor, Netzer, & Elitzur 2009; Alonso-Herrero et al. 2011; Mor & Netzer 2012; Hönig et al. 2013; Mateos et al. 2016; Hernán-Caballero et al. 2016). Various origins have been proposed for this NIR bump: 1) an extra-contribution to the nuclear fluxes from the host galaxy; 2) emission from a compact disc of hot dust detected in interferometric MIR data of some Seyfert galaxies (e.g., Hönig et al. 2013; Tristram et al. 2014); and 3) emission from a hot pure-graphite component located in the outer part of the BLR, as proposed by Mor, Netzer, & Elitzur (2009).

Regarding the latter possibility, in Mor, Netzer, & Elitzur (2009) the authors found for a sample of 26 type 1 quasars that their NIR SEDs required an extra hot dust component ($T \sim 800\text{--}1800\ \text{K}$), in addition to a clumpy torus model, to be reproduced. The widely used clumpy torus models of Nenkova et al. (2008a,b) assume a standard Galactic grain composition of 53% silicates and 47% graphites, and the sublimation temperature of silicate grains ($\sim 1500\ \text{K}$). Mor & Netzer (2012) proposed that to reproduce the NIR bump, a collection of dusty clouds of pure-graphite ($T_{sub} \sim 1800\ \text{K}$) in the outer part of the BLR is needed. This difference between the sublimation temperature of silicates and graphites has

been accounted for in the latter version of the CAT3D torus models (Hönig & Kishimoto 2010), and it explains a wider variety of SED shapes (García-González et al. in preparation). On the other hand, using MIR interferometry data of the Seyfert 1 galaxy NGC 3783, Hönig et al. (2013) proposed a different scenario to reproduce the nuclear IR SED of Seyfert galaxies. The MIR bump ($\sim 15\text{--}20\ \mu\text{m}$) would be produced by polar dust within the inner parsecs of the galaxy and the NIR bump ($\sim 1\text{--}5\ \mu\text{m}$) by a compact disc structure (i.e. the torus). The results presented here indicate that this NIR bump is strongly correlated with the hard X-rays, confirming that it is AGN-related, but we cannot favour either of the two alternative origins discussed above.

The broad energy coverage of the *NuSTAR* data studied here allows us to divide the X-ray continuum emission in a set of bands between 3 and 80 keV. We find that both the shape and the correlation strengths of the IRXCS are independent of the X-ray band chosen (see left panel of Fig. 3). In the 40–80 keV band this is probably the case as well, but the large number of upper limits prevents confirmation (see Appendix B). It is not surprising to find the same behaviour for the 3–5 keV and the 7–15 keV correlations since they are sampling the featureless AGN continuum. We might have expected a different behaviour for the 15–40 keV correlation because it includes the Compton hump, but that is not the case. A detailed spectral analysis of the *NuSTAR* data is beyond the scope of this paper, and will be presented elsewhere (Baloković et al. in preparation). However, that study shows that the contribution of the Compton hump for the galaxies in our sample is in the range 10–20%. This would be consistent with the result that we see no significant differences in the correlations between the different X-ray energy bands.

We finally studied the strength of the correlation between the X-ray and the MIR emission-line luminosities. All the lines considered show a good correlation with the X-rays ($\rho \gtrsim 0.7$), and the correlation strength does not depend on the IP of the lines (see Fig. 4). For example, the strongest correlation is found for the low-IP line [Ne II], which is commonly used as a star formation tracer in galaxies. Nevertheless, according to Meléndez et al. (2008b), this emission line in active galaxies has both AGN and star formation contributions, and the latter is likely to be insignificant in the AGN-dominated systems that make up our sample. In principle, we expected the lines with the highest IPs ([Ne V] and [O IV]) to show the strongest correlations with the X-rays, but the correlation coefficients are intermediate between those of lower IPs. As recently shown by Landt et al. (2015a,b) for the type 1 AGN NGC 4151 and NGC 5548, both included in our sample, variability in the coronal line region could be a potential source of “dilution” of the correlation coefficient strengths, explaining the results found for these high-IP lines.

8 CONCLUSIONS

In this work we apply, for the first time, the correlation spectrum technique to cross-correlate monochromatic NIR and MIR luminosities with various *NuSTAR* X-ray bands for a sample of 24 unobscured type 1 AGN. The main

results are as follows:

- The *NuSTAR* data studied here allows to divide the X-ray emission up into selected energy bands between 3 and 80 keV. We find both the shape of the IRXCS and the correlation strengths independent of the X-ray band selected, although the large number of upper limits in the 40–80 keV band prevents confirmation at the highest energies. The same situation is apparent when considering the emission line correlations.

- We find the IRXCS correlation maximum at $\sim 15\text{--}20\ \mu\text{m}$. This peak coincides with the maximum contribution of the AGN to the IRS spectra analyzed here. At $\lambda \gtrsim 20\ \mu\text{m}$ the correlation spectrum slowly decreases.

- We find a NIR correlation peak at $\sim 2\ \mu\text{m}$, which we associate with the NIR bump observed in the SEDs of some type 1 AGN at $\sim 1\text{--}5\ \mu\text{m}$. The results presented here indicate that this correlation feature is produced by AGN-heated dust.

- All the MIR emission lines considered here, whose IPs range from 8 to 97 eV, show a good correlation with the hard X-rays ($\rho \gtrsim 0.7$). It is noteworthy that the correlation strength does not depend on the IP of the lines.

Detailed studies such as this, carried out across the whole NIR-MIR spectral range, are clearly complementary to very large statistical studies, for example Chen et al. (2017), which focus on specific X-ray and IR bands, but with wider luminosity and redshift coverage. In the future the spectral correlation technique may be applied to AGN samples observed with the combined spectral coverage of NIRSpect and MIRI aboard the *James Webb Space Telescope* (*JWST*).

ACKNOWLEDGMENTS

IGB acknowledges financial support from the Instituto de Astrofísica de Canarias through Fundación La Caixa. IGB also acknowledges the Durham University for their hospitality during his stay in March and April 2015 when this project was started. CRA acknowledges the Ramón y Cajal Program of the Spanish Ministry of Economy and Competitiveness through project RYC-2014-15779. M.B. acknowledges support from NASA Headquarters under the NASA Earth and Space Science Fellowship Program, grant NNX14AQ07H. We finally acknowledge useful comments from the anonymous referee.

REFERENCES

Alonso-Herrero A., et al., 2011, *ApJ*, 736, 82
 Alonso-Herrero A., et al., 2014, *MNRAS*, 443, 2766
 Antonucci R., 1993, *ARA&A*, 31, 473
 Arnaud K. A., 1996, *ASPC*, 101, 17
 Asmus D., Gandhi P., Hönig S. F., Smette A., Duschl W. J., 2015, *MNRAS*, 454, 766
 Awaki H., Koyama K., Inoue H., Halpern J. P., 1991, *PASJ*, 43, 195
 Ballantyne D. R., et al., 2014, *ApJ*, 794, 62
 Baloković M., et al., 2014, *ApJ*, 794, 111

Bassani L., Dadina M., Maiolino R., Salvati M., Risaliti G., Della Ceca R., Matt G., Zamorani G., 1999, *ApJS*, 121, 473
 Brenneman L. W., et al., 2014, *ApJ*, 788, 61
 Cappi M., et al., 2006, *A&A*, 446, 459
 Chen C.-T. J., et al., 2017, arXiv, arXiv:1701.05207
 Corral A., Della Ceca R., Caccianiga A., Severgnini P., Brunner H., Carrera F. J., Page M. J., Schwobe A. D., 2011, *A&A*, 530, A42
 Dadina M., 2008, *A&A*, 485, 417
 Dasyra K. M., Ho L. C., Netzer H., Combes F., Trakhtenbrot B., Sturm E., Armus L., Elbaz D., 2011, *ApJ*, 740, 94
 de Rosa A., Piro L., Perola G. C., Capalbi M., Cappi M., Grandi P., Maraschi L., Petrucci P. O., 2007, *A&A*, 463, 903
 Diamond-Stanic A. M., Rieke G. H., Rigby J. R., 2009, *ApJ*, 698, 623
 Diamond-Stanic A. M., Rieke G. H., 2012, *ApJ*, 746, 168
 Dickey J. M., Lockman F. J., 1990, *ARA&A*, 28, 215
 Elitzur M., 2012, *ApJ*, 747, L33
 Esquej P., et al., 2014, *ApJ*, 780, 86
 Feigelson E. D., Nelson P. I., 1985, *ApJ*, 293, 192
 Fiore F., et al., 2009, *ApJ*, 693, 447
 Gandhi P., Horst H., Smette A., Hönig S., Comastri A., Gilli R., Vignali C., Duschl W., 2009, *A&A*, 502, 457
 García-Bernete I., et al., 2015, *MNRAS*, 449, 1309
 García-Bernete I., et al., 2016, *MNRAS*, 463, 3531
 George I. M., Fabian A. C., 1991, *MNRAS*, 249, 352
 Gorjian V., Cleary K., Werner M. W., Lawrence C. R., 2007, *ApJ*, 655, L73
 Haardt F., Maraschi L., 1991, *ApJ*, 380, L51
 Hao L., et al., 2005, *ApJ*, 625, L75
 Harrison F. A., et al., 2013, *ApJ*, 770, 103
 Hatziminaoglou E., Hernán-Caballero A., Feltre A., Piñol Ferrer N., 2015, *ApJ*, 803, 110
 Hernán-Caballero A., et al., 2015, *ApJ*, 803, 109
 Hernán-Caballero A., Hatziminaoglou E., Alonso-Herrero A., Mateos S., 2016, *MNRAS*, 463, 2064
 Ho L. C., Keto E., 2007, *ApJ*, 658, 314
 Hönig S. F., Kishimoto M., 2010, *A&A*, 523, A27
 Hönig S. F., et al., 2013, *ApJ*, 771, 87
 Hopkins P. F., Quataert E., 2010, *MNRAS*, 407, 1529
 Horst H., Gandhi P., Smette A., Duschl W. J., 2008, *A&A*, 479, 389
 Houck J. R., et al., 2004, *ApJS*, 154, 18
 Howarth I. D., Murray J., Mills D., Berry D. S., 2004, *StAUN*, 50,
 Ichikawa K., Ueda Y., Terashima Y., Oyabu S., Gandhi P., Matsuta K., Nakagawa T., 2012, *ApJ*, 754, 45
 Ichikawa K., Ricci C., Ueda Y., Matsuoka K., Toba Y., Kawamuro T., Trakhtenbrot B., Koss M. J., 2017, *ApJ*, 835, 74
 Isobe T., Feigelson E. D., Nelson P. I., 1986, *ApJ*, 306, 490
 Jin C., Ward M., Done C., 2012, *MNRAS*, 422, 3268
 Jovanović P., Zakharov A. F., Popović L. Č., Petrović T., 2008, *MNRAS*, 386, 397
 Koike C., Shibai H., Tuchiya A., 1993, *MNRAS*, 264, 654
 Kotilainen J. K., Ward M. J., Boisson C., Depoy D. L., Smith M. G., Bryant L. R., 1992, *MNRAS*, 256, 125
 Koss M. J., et al., 2015, *ApJ*, 807, 149

- Krabbe A., Böker T., Maiolino R., 2001, *ApJ*, 557, 626
 Lamperti I., et al., 2017, *MNRAS*, in press
 Landt H., Buchanan C. L., Barmby P., 2010, *MNRAS*, 408, 1982
 Landt H., Bentz M. C., Ward M. J., Elvis M., Peterson B. M., Korista K. T., Karovska M., 2008, *ApJS*, 174, 282
 Landt H., Elvis M., Ward M. J., Bentz M. C., Korista K. T., Karovska M., 2011, *MNRAS*, 414, 218
 Landt H., Ward M. J., Peterson B. M., Bentz M. C., Elvis M., Korista K. T., Karovska M., 2013, *MNRAS*, 432, 113
 Landt H., Ward M. J., Steenbrugge K. C., Ferland G. J., 2015a, *MNRAS*, 449, 3795
 Landt H., Ward M. J., Steenbrugge K. C., Ferland G. J., 2015b, *MNRAS*, 454, 3688
 Lansbury G. B., et al., 2017, submitted
 Lebouteiller V., Barry D. J., Spoon H. W. W., Bernard-Salas J., Sloan G. C., Houck J. R., Weedman D. W., 2011, *ApJS*, 196, 8
 Levenson N. A., Radomski J. T., Packham C., Mason R. E., Schaefer J. J., Telesco C. M., 2009, *ApJ*, 703, 390
 Lohfink A. M., et al., 2015, *ApJ*, 814, 24
 Lutz D., Maiolino R., Spoon H. W. W., Moorwood A. F. M., 2004, *A&A*, 418, 465
 Madsen K. K., et al., 2015, *ApJS*, 220, 8
 Masini A., et al., 2016, *A&A*, 589, A59
 Mason R. E., et al., 2012, *AJ*, 144, 11
 Mateos S., et al., 2015, *MNRAS*, 449, 1422
 Mateos S., et al., 2016, *ApJ*, 819, 166
 Matsuta K., et al., 2012, *ApJ*, 753, 104
 Meléndez M., et al., 2008a, *ApJ*, 682, 94
 Meléndez M., Kraemer S. B., Schmitt H. R., Crenshaw D. M., Deo R. P., Mushotzky R. F., Bruhweiler F. C., 2008b, *ApJ*, 689, 95-107
 Mor R., Netzer H., Elitzur M., 2009, *ApJ*, 705, 298
 Mor R., Netzer H., 2012, *MNRAS*, 420, 526
 Mould J. R., et al., 2000, *ApJ*, 529, 786
 Nenkova M., Sirocky M. M., Ivezić Ž., Elitzur M., 2008, *ApJ*, 685, 147
 Nenkova M., Sirocky M. M., Nikutta R., Ivezić Ž., Elitzur M., 2008, *ApJ*, 685, 160
 Packham C., Radomski J. T., Roche P. F., Aitken D. K., Perlman E., Alonso-Herrero A., Colina L., Telesco C. M., 2005, *ApJ*, 618, L17
 Peeters E., Spoon H. W. W., Tielens A. G. G. M., 2004, *ApJ*, 613, 986
 Pereira-Santaella M., Alonso-Herrero A., Rieke G. H., Colina L., Díaz-Santos T., Smith J.-D. T., Pérez-González P. G., Engelbracht C. W., 2010a, *ApJS*, 188, 447
 Pereira-Santaella M., Diamond-Stanic A. M., Alonso-Herrero A., Rieke G. H., 2010, *ApJ*, 725, 2270
 Pier E. A., Krolik J. H., 1992, *ApJ*, 401, 99
 Prieto M. A., Pérez García A. M., Rodríguez Espinosa J. M., 2002, *MNRAS*, 329, 309
 Radomski J. T., Piña R. K., Packham C., Telesco C. M., De Buizer J. M., Fisher R. S., Robinson A., 2003, *ApJ*, 587, 117
 Ramos Almeida C., Pérez García A. M., Acosta-Pulido J. A., Rodríguez Espinosa J. M., 2007, *AJ*, 134, 2006
 Ramos Almeida C., et al., 2014, *MNRAS*, 445, 1130
 Rayner J. T., Toomey D. W., Onaka P. M., Denault A. J., Stahlberger W. E., Vacca W. D., Cushing M. C., Wang S., 2003, *PASP*, 115, 362
 Ricci C., Walter R., Courvoisier T. J.-L., Paltani S., 2011, *A&A*, 532, A102
 Riffel R., Rodríguez-Ardila A., Pastoriza M. G., 2006, *A&A*, 457, 61
 Rigby J. R., Diamond-Stanic A. M., Aniano G., 2009, *ApJ*, 700, 1878
 Rodríguez-Ardila A., Viegas S. M., Pastoriza M. G., Prato L., 2002, *ApJ*, 579, 214
 Ruschel-Dutra D., Pastoriza M., Riffel R., Sales D. A., Winge C., 2014, *MNRAS*, 438, 3434
 Sales D. A., Pastoriza M. G., Riffel R., Winge C., 2013, *MNRAS*, 429, 2634
 Sazonov S., et al., 2012, *ApJ*, 757, 181
 Shi Y., et al., 2006, *ApJ*, 653, 127
 Singh V., Shastri P., Risaliti G., 2011, *A&A*, 532, A84
 Skrutskie M. F., et al., 2006, *AJ*, 131, 1163
 Smith D. A., Done C., 1996, *MNRAS*, 280, 355
 Smith J. D. T., et al., 2007, *ApJ*, 656, 770
 Spinoglio L., Malkan M. A., 1992, *ApJ*, 399, 504
 Spinoglio L., Dasyra K. M., Franceschini A., Gruppioni C., Valiante E., Isaak K., 2012, *ApJ*, 745, 171
 Sturm E., Lutz D., Tran D., Feuchtgruber H., Genzel R., Kunze D., Moorwood A. F. M., Thornley M. D., 2000, *A&A*, 358, 481
 Tristram K. R. W., Burtscher L., Jaffe W., Meisenheimer K., Hönig S. F., Kishimoto M., Schartmann M., Weigelt G., 2014, *A&A*, 563, A82
 Turner T. J., George I. M., Nandra K., Mushotzky R. F., 1997, *ApJS*, 113, 23
 Ursini F., et al., 2016, *MNRAS*, 463, 382
 Waters L. B. F. M., et al., 1998, *A&A*, 331, L61
 Wu H., Cao C., Hao C.-N., Liu F.-S., Wang J.-L., Xia X.-Y., Deng Z.-G., Young C. K.-S., 2005, *ApJ*, 632, L79
 Zoghbi A., et al., 2015, *ApJ*, 799, L24

APPENDIX A: SPECTRAL DECOMPOSITION

Here we show the *Spitzer/IRS* spectra of our sample of 24 unobscured type 1 AGN, which were retrieved from the CASIS atlas (Lebouteiller et al. 2011). Considering the spatial scales probed ($0.2 \text{ kpc} \lesssim \text{spatial scale} \lesssim 5.4 \text{ kpc}$), we expect some degree of contribution from the host galaxy to the MIR spectra, in addition to the AGN. To estimate these contributions, we use the *DeblendIRS* routine (Hernán-Caballero et al. 2015), that decomposes MIR spectra using a linear combination of three spectral components: AGN, PAH and stellar emission. The spectrum of each component is selected from a large library containing *Spitzer/IRS* spectra from extreme cases of galaxies dominated by AGN, PAH, or stellar emission. Note that we have consistently avoided the use of the sources themselves as templates, since few of our galaxies are in the AGN library of *DeblendIRS*. Due to limitations in the library, we cannot expand the spectral decomposition beyond $22 \mu\text{m}$. A detailed description of the method is given in Hernán-Caballero et al. (2015), which we already tested in García-Bernete et al. (2016).

We present the main results and properties derived from the spectral decomposition of our sample in Fig. A1 and Table A1. We found that the median value of the fractional contribution of the AGN to the *Spitzer/IRS* spectra is 0.90,

as expected for type 1 AGN. For the majority of the galaxies we find the maximum of the fitted AGN template at 20–25 μm . Note that in the case of NGC 7213 we cannot obtain a reliable fit, as the modelling does not reproduce the 9.7 μm silicate emission feature.

APPENDIX B: CORRELATION SPECTRA

As a sanity check we repeated the correlation spectra for the 2–10, 7–15, 15–40 and 40–80 keV bands, but only using the subsample of 15 sources without upper limits in the 40–80 keV band (see Table 2 in Section 3.1). We found that the IR–X-ray correlations are practically identical in all the X-ray bands considered here (see Fig. B1). Therefore, we conclude that the lower significance found for the 40–80 keV IRXCS when the whole sample is considered (see bottom-right panel of Fig. 2) is due to the large number of upper limits included and not a real feature.

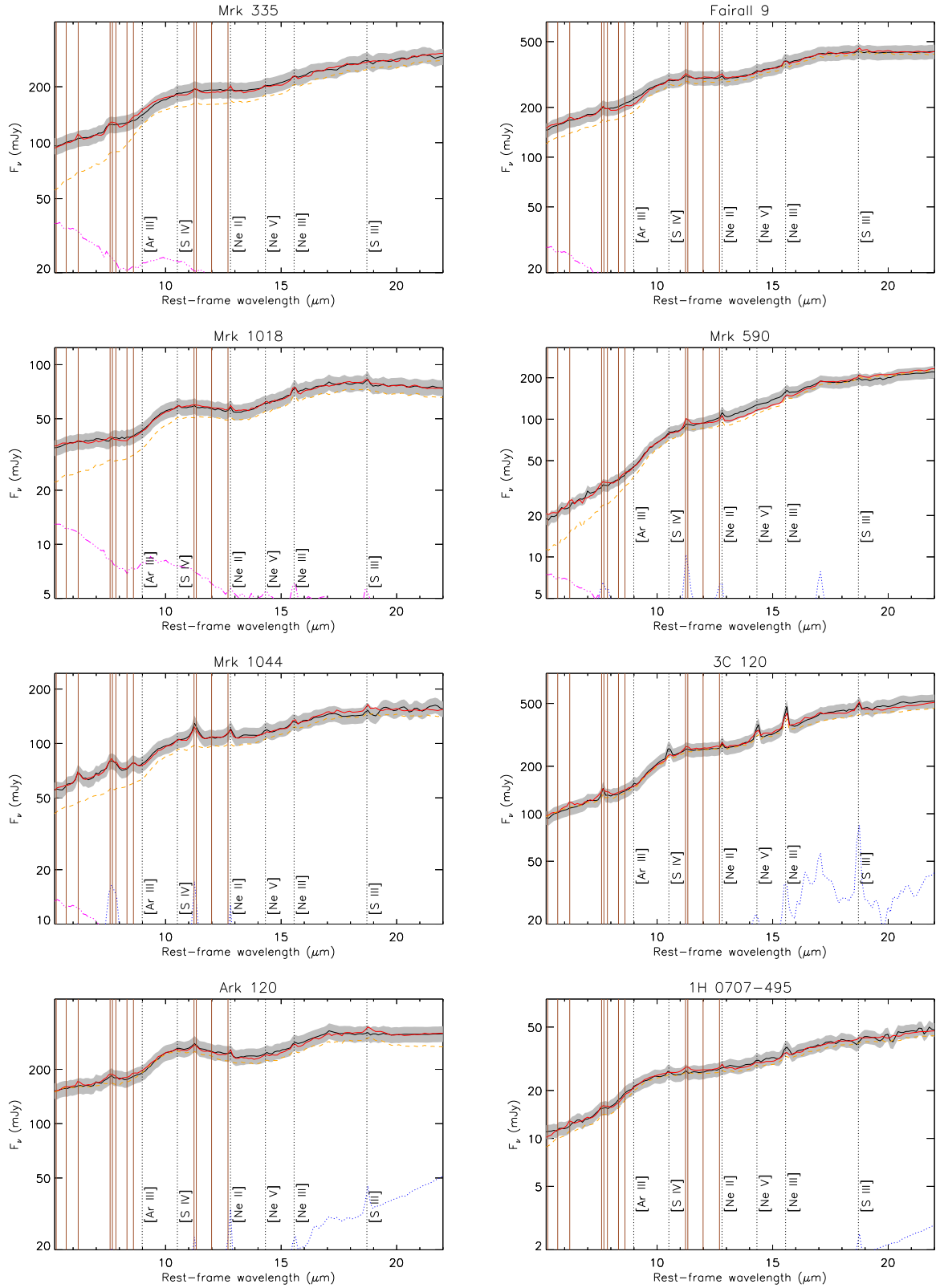


Figure A1. Spectral decomposition of the *Spitzer/IRS* spectra of our sample. We show the rest-frame spectra (black solid lines), best fits (red solid lines), AGN component (orange dashed lines), PAH component (blue dotted lines) and stellar component (dot-dashed fuchsia lines). The brown vertical solid lines correspond to the most important PAH features and the black vertical dotted lines are the main MIR emission lines. The uncertainties of the *Spitzer/IRS* spectra are shown as grey shaded regions.

Figure A1 – continued

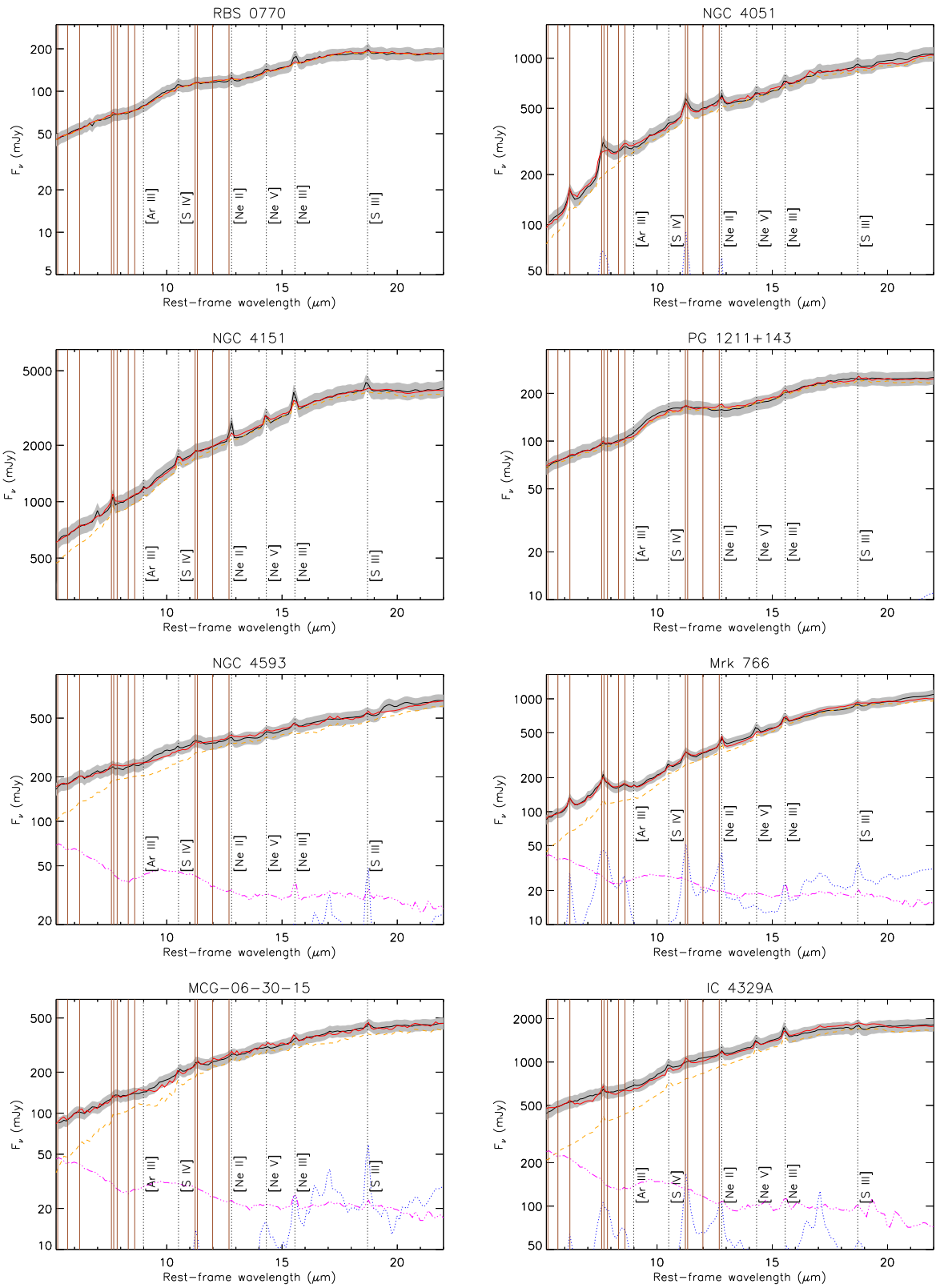
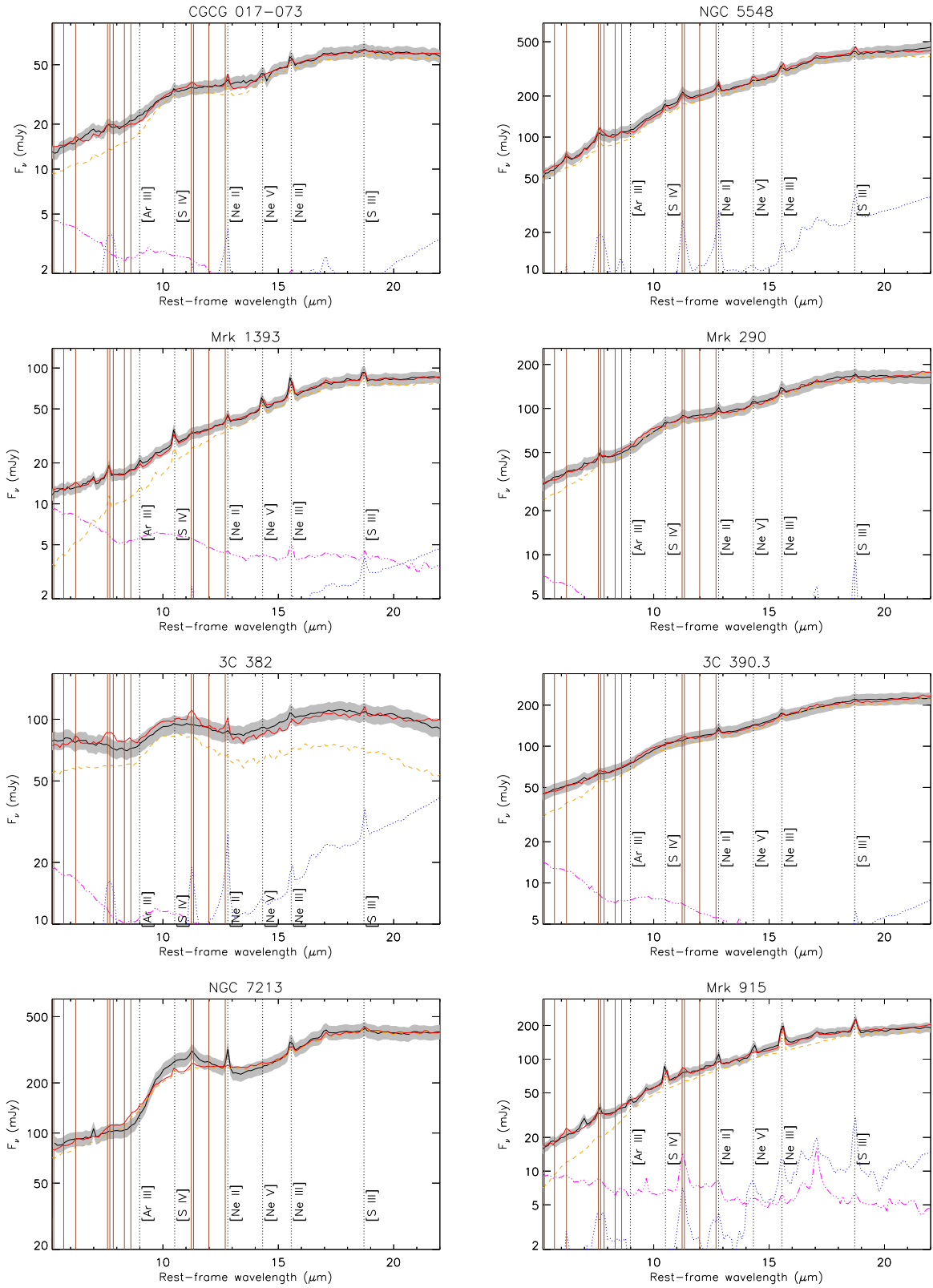


Figure A1 – *continued*

Name	F_{AGN}	F_{PAH}	$F_{Stellar}$	α_{AGN}	S_{Si}	$F_{6\mu m}^{AGN}$	$F_{12\mu m}^{AGN}$	$F_{20\mu m}^{AGN}$
Mrk 335	0.82	0.04	0.14	-1.30	0.25	0.64	0.86	0.92
Fairall 9	0.91	0.02	0.07	-1.22	0.19	0.82	0.94	0.97
Mrk 1018	0.83	0.02	0.15	-1.16	0.24	0.67	0.88	0.90
Mrk 590	0.88	0.05	0.07	-2.74	0.32	0.59	0.92	0.98
Mrk 1044	0.85	0.06	0.09	-1.22	0.19	0.75	0.89	0.93
3C 120	0.96	0.04	0.00	-1.62	0.18	0.97	0.97	0.95
Ark 120	0.95	0.05	0.00	-0.64	0.28	0.98	0.95	0.88
1H 0707-495	0.94	0.03	0.03	-1.30	0.25	0.89	0.95	0.94
RBS 0770	0.99	0.01	0.00	-1.24	0.12	0.99	1.00	0.99
NGC 4051	0.91	0.07	0.02	-1.75	0.07	0.83	0.92	0.97
NGC 4151	0.93	0.02	0.05	-1.86	0.03	0.81	0.95	0.96
PG 1211+143	0.97	0.02	0.01	-1.22	0.19	0.96	0.98	0.96
NGC 4593	0.84	0.01	0.15	-1.19	-0.03	0.65	0.89	0.92
Mrk 766	0.83	0.07	0.10	-2.27	-0.17	0.57	0.88	0.95
MCG-06-30-015	0.82	0.03	0.15	-1.91	-0.19	0.54	0.88	0.92
IC 4329A	0.77	0.06	0.17	-1.86	0.03	0.49	0.82	0.93
CGCG 017-073	0.86	0.05	0.09	-1.75	0.29	0.69	0.90	0.94
NGC 5548	0.92	0.06	0.02	-1.86	0.06	0.88	0.93	0.93
Mrk 1393	0.77	0.03	0.20	-2.67	-0.09	0.35	0.84	0.91
Mrk 290	0.93	0.01	0.06	-1.66	0.17	0.80	0.96	0.97
3C 382	0.77	0.10	0.13	-0.30	0.33	0.74	0.79	0.63
3C 390.3	0.90	0.02	0.08	-1.66	0.17	0.73	0.93	0.96
NGC 7213	0.96	0.00	0.04	-1.92	0.33	0.90	0.97	0.98
Mrk 915	0.84	0.04	0.12	-2.79	0.20	0.53	0.88	0.93

Table A1. Properties derived from the spectral decomposition of the *Spitzer/IRS* spectra of the sample. Columns 2, 3 and 4 correspond to the fractional contribution of the AGN, the PAH and the stellar components to the MIR spectrum. Columns 5 and 6 list the spectral index of the AGN component and the silicate strength (positive and negative values correspond to emission and absorption features, respectively). Finally, columns 7 and 9 correspond to the fractional contribution of the AGN component to the rest-frame spectrum at 6 μm , 12 μm and 20 μm , respectively.

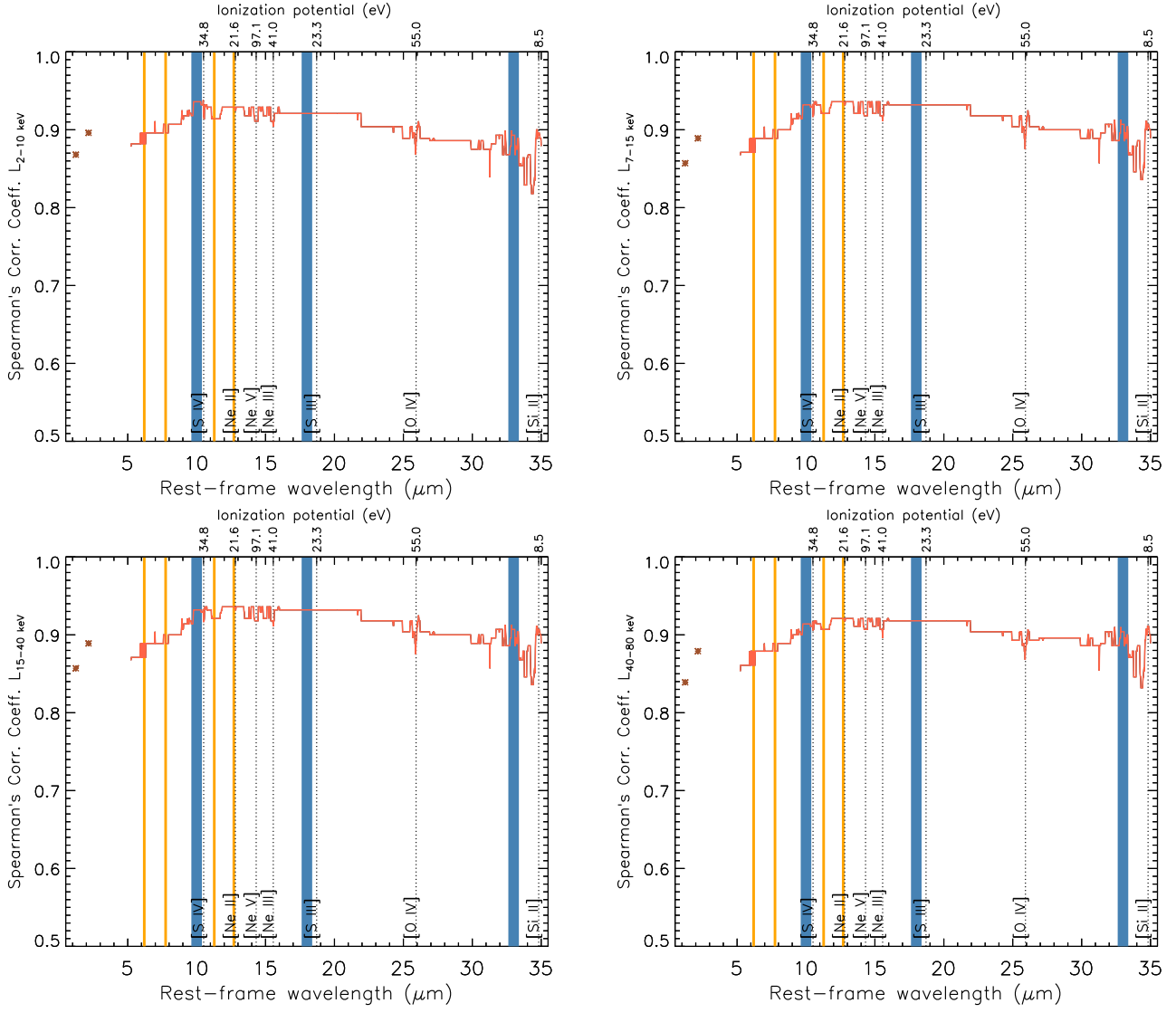


Figure B1. Same as in Fig. 2 but for the subsample of 15 sources without upper limits in the 40-80 keV band.